JGR Space Physics

RESEARCH ARTICLE
10.1029/2025JA033966

# A Comparison of Modeled and Observed Dayside Bow Shock Locations in 8 Years of MMS Data

**Wenli Mo[1], Savvas Raptis[1], Vicki Toy-Edens[1], Kiley Yeakel[1], and Drew L. Turner[1]**

[1]Johns Hopkins University Applied Physics Laboratory, Laurel, MD, USA

**Key Points:**

- We refine existing bow shocks models using new MMS observations, improving their initial goodness-of-fit by up to 17%
- Discrepancies between bow shock models and observations occur during periods of extreme solar wind conditions
- Quasi-parallel and quasi-perpendicular bow shocks exhibit systematic differences in standoff distance and spatial distribution

**Supporting Information:**

Supporting Information may be found in the online version of this article.

**Correspondence to:**

W. Mo,
wenli.mo@jhuapl.edu

**Citation:**

Mo, W., Raptis, S., Toy-Edens, V., Yeakel, K., & Turner, D. L. (2025). A comparison of modeled and observed dayside bow shock locations in 8 Years of MMS data. *Journal of Geophysical Research: Space Physics*, *130*, e2025JA033966. https://doi.org/10.1029/2025JA033966

Received 13 MAR 2025
Accepted 13 OCT 2025



**Abstract** The interplay between Earth's magnetic field and the solar wind provides a natural laboratory to study the physics of shock waves in collisionless plasmas. 3D parameterized shape models of Earth's bow shock boundary quantify how this interaction depends on upstream solar wind parameters. Using 2,063 bow shocks observed with the Magnetospheric Multiscale (MMS) mission over 8 years, we investigate the relationship between the observed and parameterized bow shock location with solar wind parameters. We find that the observed bow shock location is strongly correlated with the solar wind density, plasma $\beta$, and Mach number. In addition, we provide updated fitting parameters to bow shock models from literature derived empirically or using magnetohydrodynamic (MHD) simulations. Models provide a reasonable fit to the data after updating the fit with MMS-observed bow shocks, with coefficient of determination $(R^2)$ scores between 0.836–0.878. However, we find that observed locations can still deviate significantly from model predictions under extreme solar wind conditions. We also explore the models' variability under different interplanetary magnetic field (IMF) clock angles (Northward and Southward) and shock geometries (quasi-perpendicular and quasi-parallel). While we observe no discernible difference in the bow shock shape as a function of IMF direction, we find that quasi-parallel bow shocks are systematically closer to Earth than quasi-perpendicular, with a disparity of as much as $\sim 1\ R_E$ in bow shock stand-off distance between the two bow shock types.

## 1. Introduction

Interplanetary space is flooded by a continual, turbulent stream of plasma emitted by the Sun: the solar wind. Within the solar corona, very near the Sun, the solar wind is heated and accelerated to the point that it becomes super-fast-magnetosonic, that is, moving faster than the fastest magnetohydrodynamic (MHD) wave modes that exist within it. Earth, surrounded by its internally driven magnetic field, acts as an obstacle around which the solar wind must divert and flow, and in the process of doing so, a shock wave forms to regulate the transition between super-fast-magnetosonic (and also super-Alfvénic) and sub-fast, sub-Alfvénic flow around Earth's magnetopause. This shock transition is an intriguing and important boundary since collisionless shocks are ubiquitous in space plasmas and are considered one of the most important accelerators of very high energy (up to relativistic) particles in the Solar System and other astrophysical plasmas (Balogh & Treumann, 2013; Treumann, 2009). Beyond that, the Earth's bow shock forms under a range of upstream solar wind plasma conditions, making it an excellent natural laboratory to directly study the physics of shock waves in collisional plasmas.

The size, scale and shape (e.g., curved vs. planar) of collisionless shocks are important characteristics that ultimately limit the level of acceleration of energetic particles at shocks (Perri et al., 2022). There are two prevailing methods of determining the terrestrial bow shock shape. One is using global MHD or hybrid modeling of the interaction of the solar wind with the Earth's magnetic field (Battarbee et al., 2020; Merka et al., 2003). Simulations offer the advantage of modeling bow shocks across a wide range of solar wind conditions and allow the generation of a full shock geometry. Alternatively, another method to determine the shape of the terrestrial bow shock is empirical, relying on actual observations of the location of the shock transition layer in satellite data (e.g., Chao et al., 2002; Jelínek et al., 2012). In situ observations provide a more accurate representation of real conditions but are inherently sparse, offering valuable local insights while limiting global coverage unless analyzed systematically across various driving conditions.

Bow shock models are valuable to the heliophysics research community for a number of reasons. Analytical fitting models parameterized by upstream conditions (e.g., Chapman & Cairns, 2003) offer users approachable and computationally light tools to determine where the bow shock is located at any given time, under any particular upstream (i.e., in the solar wind) conditions. Such models offer an approach to determine if a satellite may be located within Earth's magnetosheath or in the solar wind or to associate a bow shock normal direction to a

set of local in situ observations upstream or downstream of the bow shock (e.g., Turner et al., 2021). Furthermore, previous studies have employed models to calculate distances of magnetosheath measurements from a nearby shock crossing to evaluate temporal and spatial evolution of transients (e.g., LaMoury et al., 2021; Raptis et al., 2020). Alternatively, models can be applied to determine local parameters of shocks when single spacecraft are present and multi-spacecraft techniques cannot be performed (e.g., Karlsson et al., 2021).

In this analysis, we use bow shocks identified in 8 years of observations by NASA's Magnetospheric Multiscale (MMS) mission. We fit the observed bow shocks to three different parameterizations of the bow shock shape, developed either by using MHD simulations or through observations from multiple in situ bow shock crossings. Furthermore, statistics using the MMS shock database and new, parameterized model bow shock fits are presented. Section 2 describes the data sets used and how bow shocks were identified within the MMS data. Section 3 compares the three bow shock models and new fits to those models using the new MMS data set. Section 4 discusses the results and their implications, while Section 5 summarizes the results and presents our conclusions. Section 6 describes how interested readers may access our data set, software, and results through the open data policy.

## 2. Data

The MMS mission, consisting of 4 identical spacecraft organized in a tetrahedron constellation, launched into orbit around Earth in March 2015 and started collecting scientific data in September 2015 (Burch et al., 2015). Many studies have provided detailed classifications of near-Earth plasma regions using in situ MMS observations, applying a variety of automated or machine learning methods (e.g., Lalti et al., 2022; Nguyen et al., 2022; Toy-Edens et al., 2024). In this study, we used classifications of dayside ($X > 0$) plasma regions presented in Toy-Edens et al. (2024, hereafter T24). T24 applied an unsupervised Gaussian Mixture Model clustering method on features extracted from Level 2 science data from the Fast Plasma Investigation (FPI, Pollock et al., 2016) Dual Ion Spectrometer and the Fluxgate Magnetometers (FGM, Torbert et al., 2014), as well as implemented a spacecraft location filter with the Magnetic Ephemeris and Coordinates (MEC, Henderson et al., 2022) data product. Specifically, T24 used the ion energy spectra from the FPI DIS moments data product to extract clustering features for initial clustering labels, then performed post-cleaning of the labels using additional information from the ion density, temperature, velocity, and the magnetic field.

T24 distinguished between magnetosphere, magnetosheath, solar wind, and ion foreshock plasma regions in MMS data between September 2015 and January 2024, consisting of 66,498 hr of data in total spanning all four spacecraft on Earth's dayside at a standard 1-min temporal cadence. Comparing to a data set of hand-labeled plasma regions from Olshevsky et al. (2021), T24 reported a 97.8% match rate.

Throughout our analysis, we will use both Geocentric Solar Ecliptic (GSE) and Geocentric Solar Magnetospheric (GSM) coordinates. We specify the coordinate system as a subscript.

### 2.1. Bow Shock Catalog

The T24 data set includes bow shock and magnetopause transitions extracted from the MMS in situ plasma region identification. A quasi-parallel bow shock was defined as when MMS transitions from an ion foreshock classification to magnetosheath, or vice versa, and a quasi-perpendicular bow shock was when the classification transitions from solar wind to magnetosheath, or vice versa. Over four MMS probes, T24 found 26,221 total bow shocks. However, each bow shock has an equal probability of being observed with any of the four probes. Therefore, we only considered the 6,604 bow shocks observed by MMS1 in this analysis.

We used the T24 data set as a baseline of potential transitions in MMS and further cleaned bow shocks to those most suitable for our analysis. First, we determined the upstream and downstream sides of the bow shock using the T24 clustering labels. We considered the T24 labels at the 3-min period before and after the shock, avoiding the minute that the shock was identified. The upstream side is where the majority of T24 labels during the 3-min window was "solar wind" or "ion foreshock" and the downstream side is where the majority of labels within the 3-min window was "magnetosheath." For the bow shocks where upstream/downstream sides could be determined, we calculate the median values of the magnetic field magnitude and ion number density during the 3-min window on either side. We were able to determine upstream and downstream values for 5,165 bow shocks.

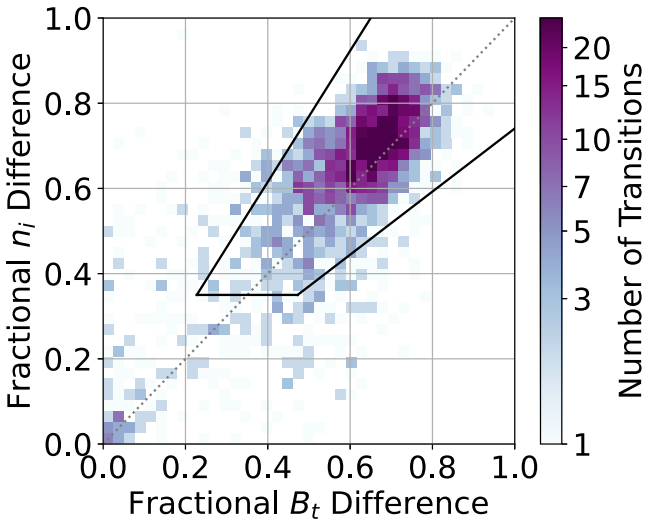


**Figure 1.** The distribution of the fractional difference in ion density $\frac{\Delta n_i}{n_i}$ as a function of fractional differential increase in the total magnetic field $\frac{\Delta B_t}{B_t}$ for 6,604 candidate bow shock transitions for MMS1 from T24. The solid black lines represent the criteria applied to filter for representative bow shocks. Bow shocks within the criteria are selected for further analysis in this work (see Section 2.1).

Using the bow shock's upstream and downstream total magnetic field, we considered the fractional change in the total magnetic field

$$\frac{\Delta B_t}{B_t} = \frac{(B_{t,dn} - B_{t,up})}{B_{t,dn}}, \quad (1)$$

where $B_{t,dn}$ and $B_{t,up}$ are the median value for magnetic field magnitude during the downstream and upstream time windows, respectively. Similarly, the fractional change in the number density is

$$\frac{\Delta n_i}{n_i} = \frac{(n_{i,dn} - n_{i,up})}{n_{i,dn}}, \quad (2)$$

where $n_{i,dn}$ and $n_{i,up}$ are downstream and upstream median ion number densities. Figure 1 shows the corresponding equations and the spread of bow shock candidates in $B_t$ versus $n_i$ fractional difference space. Shock transitions according to Rankine-Hugoniot relations (Baumjohann & Treumann, 1996) should have a jump in ion density and magnetic field as measured from upstream to downstream. This is particularly true for the shocks observed close to the subsolar region. By the definitions in Equations 1 and 2, the expected, ideal level of both $\Delta n_i/n_i$ and $\Delta B_t/B_t$ should be 0.75. We found a large grouping of bow shock candidates near $\Delta n_i/n_i = 0.75$ and $\Delta B_t/B_t = 0.75$, as expected based on the Rankine-Hugoniot jump conditions, a smaller grouping near $\Delta B_t/B_t = 0.1$ and $\Delta n_i/n_i = 0.1$, as well as spread off the one-to-one relationship between $\Delta B_t/B_t$ and $\Delta n_i/n_i$. By visual inspection, we determined the 0.75 grouping to be actual bow shocks while the smaller grouping at 0.1 is comprised of misclassifications of the clustering. These misclassifications could be physical, for example, foreshock transient phenomena, where the solar wind density is elevated and has similar properties to magnetosheath plasma, or even rare coronal mass ejections (CMEs). These, along with non-physical bow shock misclassifications, were filtered out using the relationship in Equations 1 and 2.

In Figure 1, the solid black lines mark the rules to distinguish between our desired bow shocks and non-bow shocks. The specific criteria we used were.

1. $\frac{\Delta n_i/n_i}{\Delta B_t/B_t} \geq 1.3$
2. $\frac{\Delta n_i/n_i}{\Delta B_t/B_t} \leq 0.7$
3. $\Delta n_i/n_i \geq 0.35$.

These rules were determined via visual inspection and targeted the large grouping of bow shock candidates between $\Delta B_t/B_t = 0.75$ and $\Delta n_i/n_i = 0.75$. We found 3,038 bow shocks that were contained within this criteria.

Additionally, we cleaned for other physical phenomena that may have been misclassified as bow shocks. Magnetopause boundary layers are regions of turbulence and mixing between the magnetosphere and magnetosheath. Due to the mixing nature of this region, the classifications can be confused for ion foreshock and/or solar wind, and trigger a misidentified bow shock. To clean the data set of boundary layers, we considered the 1-min resolution classifications of the plasma regions ±3 minutes around a marked bow shock transition. If there was a classification of magnetosphere within the ±3-minute time window around a bow shock, we marked that as a potential boundary layer observation and excluded it from our analysis. Overall, we found 187 bow shock transitions that matched the boundary layer criteria, but only an additional 20 bow shocks beyond the $\Delta n_i/n_i$ and $\Delta B_t/B_t$ criteria.

Finally, MMS often observes many bow shocks in quick succession, especially as the spacecraft goes in and out of the bow shock boundary. However, multiple observations of bow shocks will drastically alter the number of bow shocks. Therefore, we grouped together multiple bow shocks occurring within 20 min of each other. Out of the 3,018 shocks, 1,403 were isolated crossings with no other bow shock observed within ±10 minutes. From the remaining 1,615 shocks, we find 660 bow shock groups. We chose the crossing that had the highest $\Delta n_i/n_i$ as the representative bow shock of each group. We verified for these cases that the upstream conditions were similar and

therefore one shock transition is sufficiently describing the physical picture described by the multiple crossings of MMS. Specifically, the total interplanetary magnetic field (IMF), dynamic pressure, and Mach number were between 9−10%, indicating low variation in the observed quantities. This processes produced our final bow shock catalog used in our analysis that contains a total of 2,063 bow shocks. We refer to this group of bow shocks as "All."

We also identified subsets of quasi-parallel and quasi-perpendicular bow shocks. Traditionally, quasi-parallel and quasi-perpendicular shocks are defined by the angle between the shock normal and upstream magnetic field, where $\theta_{BN} > 45°$ are quasi-perpendicular and $\theta_{BN} \leq 45°$ are quasi-parallel. However, in this work, we distinguish the two types based on the presence or absence of ion foreshock in the upstream solar wind. While not strictly identical to the $\theta_{BN}$ classification, this definition is expected to yield similar results that may also be more accurate and physically descriptive (e.g., Karlsson et al., 2021). The bow shock was labeled a quasi-perpendicular bow shock (referred to as "QPerp") if the majority of T24 classifications within the 3-min upstream window was "solar wind". Similarly, the bow shock was quasi-parallel ("QPara") if the upstream majority label was "ion foreshock." The final data set contained 969 QPerp bow shocks and 1,094 QPara bow shocks.

Figure 2 shows the distribution of locations of the different types of bow shocks defined in this study, including bow shock types defined by the IMF direction, detailed later in Section 2.2. The location of the shock transitions on $X$ and $Y$ span across a wide range of values, but are limited to mostly low latitude due to the small range in $Z$, while as expected by the orbit of the spacecraft, the distribution of observations across all points of the bow shock is not uniform. Overall, MMS spent more time around a 12 $R_E$ arc in the X-Y plane, and less time toward larger $X$, as shown in Figure 2a. There were more bow shocks observed around the subsolar point due to the MMS observing coverage. However, there was a clear shape to the bow shock from the in situ identifications of bow shock transition, with standoff distance around $\sim$20 $R_E$ and equal flaring toward dawn and dusk.

### 2.2. Solar Wind Parameters

To associate the upstream solar wind conditions to each bow shock crossing, we used the OMNI high-resolution 1-min cadence data (King & Papitashvili, 2005). OMNI is a conglomeration of observations from the ACE, Wind, IMP 8 and Geotail spacecraft that were time-shifted to the location of Earth's bow shock nose. In particular for this analysis, we used the solar wind proton density $n_p$, bulk speed $v_{sw}$, dynamic ram pressure $P_{dyn}$, components of the IMF magnetic field $B_{IMF}$, Alfvénic Mach number $M_A$, plasma beta $\beta$, and the magnetosonic Mach number $M_{ms}$.

For each bow shock transition determined in Section 2.1, we calculated an average for each solar wind parameter using a ±5-minute time window at the transition time. We used a time-averaged value instead of the value at the specific transition time to account for the uncertainty in time propagation of the OMNI data (e.g., Case & Wild, 2012; Cash et al., 2016). Furthermore, this approach allowed us to remove potential localized spikes in the measurements that do not represent typical solar wind conditions. Out of 2,069, we found 2,004 (97%) cases where OMNI data exists to calculate an average from the ±5-minute data around the transition. Specifically, 1,062 (97%) of the 1,094 QPara and 942 (97%) out of 969 QPerp had OMNI time-averaged values.

We obtained the IMF clock angle $\theta_{cl}$ from the OMNI IMF magnetic field components, defined as

$$\theta_{cl} = \tan^{-1}\left(\frac{B_{IMF,y}}{B_{IMF,z}}\right) \quad (3)$$

where $B_{IMF,y}$ and $B_{IMF,z}$ are the $y$ and $z$ components of the IMF magnetic field, respectively. By this definition, a northward IMF bow shock has $\theta_{cl} \geq 0°$ and southward IMF bow shock $\theta_{cl} < 0°$. We found 925 bow shocks with northward IMF, 892 of which had all additional OMNI upstream solar wind parameters used in this analysis. Similarly, we find 1,079 bow shocks with southward IMF where 1,056 the requisite OMNI parameters. We refer to bow shocks with northward IMF as "IMF North" and southward IMF as "IMF South." Figure 2 shows the spatial extent of observed IMF North (panels g–i) and IMF South (panels j–l) bow shocks.

## 3. Model Comparisons and Fits

A primary goal of this study was to update the parameters for bow shock shape given the new catalog of observed bow shocks from MMS. We compared the observed bow shock locations to those predicted by literature models

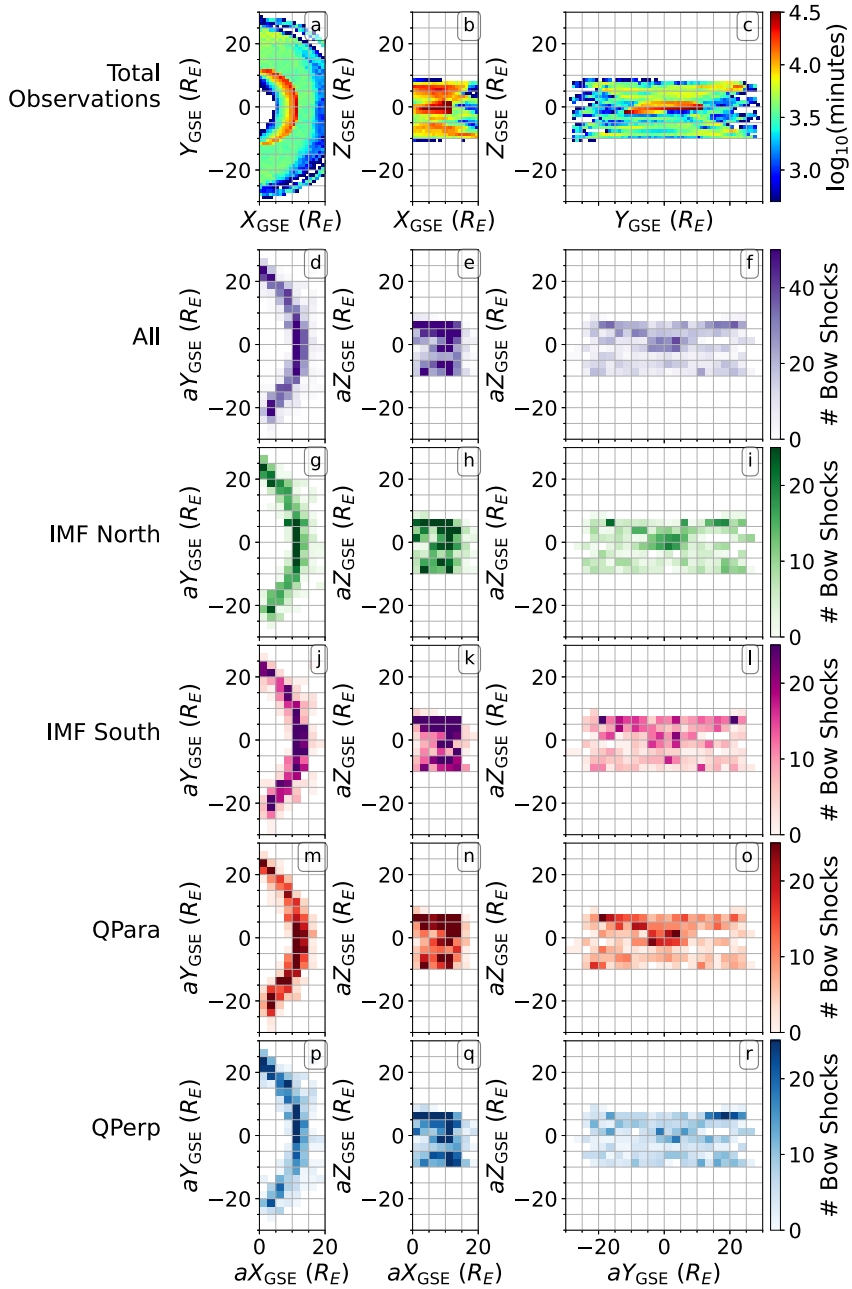


**Figure 2.** Distribution of the total observing time in minutes of MMS on dayside (rows a–c) and the number of bow shocks within each position bin in aberrated GSE coordinates for the bow shocks types analyzed in this study (see Section 2.1): All (d–f), IMF North (g–i), IMF South (j–l), QPara (m–o), and QPerp (p–r).

given the upstream solar wind conditions. First, we analyzed the statistical difference in location between observation and model and its dependence on different solar wind parameters. Then, we refitted the parameterized models to the MMS-observed bow shocks and investigated the difference in shape with different types of bow shocks (e.g., IMF North vs. IMF South, QPerp vs. QPara). We studied how the observed versus modeled bow shock location is correlated with solar wind parameters after updating the model fits to MMS bow shocks, and how the updated model performs for a different bow shock data set. Finally, we investigated example bow shocks that occurred at extreme solar wind conditions and compared how the updated models perform during these outlier times. In this study, we use the term "bow shock type" to refer to different categories of bow shocks based

on their observed characteristics. The bow shock types considered are IMF North, IMF South, QPerp, QPara, and all, as defined in Section 2.1.

### 3.1. Model Summary

We used three parameterized models of bow shock locations from literature to compare to our observed locations of bow shocks. We chose a range of models based on their derivation (e.g., MHD simulations or empirically from spacecraft observations), dependence on different solar wind conditions, and their relative complexity. We also employed a statistical simulation of the bow shock boundary parameterized by models, driven by permutations of observed solar wind conditions. A summary of each model is provided below, where we highlight the information relevant for this study. For more details on each model, we refer the reader to the original papers.

#### 3.1.1. Chapman et al. (2004) Parametric Model

Chapman and Cairns (2003) developed an empirical model of the bow shock boundary using three-dimensional ideal MHD simulations from Cairns and Lyon (1995), considering two IMF directions ($\theta_{\mathrm{IMF}} = 45°$ and $\theta_{\mathrm{IMF}} = 90°$, where $\theta_{\mathrm{IMF}}$ is defined as the angle between solar wind velocity and $B_{\mathrm{IMF}}$). Their empirical bow shock model consisted of three individual models for the bow shock flaring parameter $b_s$, the standoff distance from Earth $a_s$, and the terminator distance of the shock $L$, as a function of solar wind dynamic pressure ($P_{\mathrm{dyn}}$), Alfvénic Mach number ($M_A$), and $\theta_{\mathrm{IMF}}$.

We employed the parametrization discussed in Chapman et al. (2004), which expanded upon the Chapman and Cairns (2003) model with more $\theta_{\mathrm{IMF}}$ configurations and a consideration of the observed aberration of the bow shock shape. At location $x$, $y$, and $z$ in GSE coordinates, Chapman et al. (2004) described the location of the bow shock as

$$x = a_s - b_s r^2 \tag{4}$$

$$a_s = J + \frac{K}{M_A^2} \tag{5}$$

$$\frac{b_s}{a_s} = \frac{1}{L^2} R_E^{-2} \tag{6}$$

$$L = \left(A + \frac{B}{M_A^2}\right)\left(\frac{P_{\mathrm{dyn}}}{1.87\ \mathrm{nPa}}\right)^{-1/6} R_E \tag{7}$$

where $r = \sqrt{y^2 + z^2}$ and $J$, $K$, $A$, and $B$ are parameters to be fitted. Similar to the methodology in Chapman et al. (2004), we determined the best fit to the four parameters on the $X$–$Y$ plane assuming $\theta_{\mathrm{IMF}} = 45°$.

#### 3.1.2. Jelinek et al. (2012) Parametric Model

Jelínek et al. (2012) developed a generalized parabolic model for the shape of the bow shock and magnetopause with observed data. They used data of the in situ plasma regions observed over 5 orbits by THEMIS as the spacecraft moved through Earth's magnetosphere, magnetosheath and solar wind plasma regions. They paired the plasma observations with upstream solar wind parameters from the ACE spacecraft, specifically the IMF magnetic field magnitude, density, dynamic pressure, and velocity. Using ratios of the magnetic field and density from THEMIS and ACE, Jelínek et al. (2012) was able to identify THEMIS magnetopause and bow shock transitions between a range of magnetic local time (MLT) between 5 and 19 hr for radial distances larger than 5 $R_E$. The THEMIS observations were limited to low latitude bow shocks only, so the Jelínek et al. (2012) model assumed rotational symmetry about the $X$ axis.

To obtain the bow shock boundary, Jelínek et al. (2012) assumed that the bow shock shape is only dictated by the upstream solar wind pressure ($P_{\mathrm{dyn}}$) and computed the likelihood of finding the solar wind or magnetosheath in each location, binning by aberrated GSE coordinates given a pressure value. They then used a least-squares algorithm to solve for the mean positions of the bow shock as a paraboloid, depending on a fitting parameter

$R_0$ and a pressure factor $\epsilon$. For a location X, Y, Z in the aberrated GSE frame, the bow shock surface can be parameterized as

$$\tau = \sqrt{\sqrt{X^2 + (\lambda Y)^2 + (\lambda Z)^2} - X} \tag{8}$$

$$X = R_0 {P_{\mathrm{dyn}}}^{-1/\epsilon} - \tau^2/2 \tag{9}$$

where $R_0$, $\epsilon$ and $\lambda$ are the parameters to be fitted. The standoff distance is then calculated as

$$R_{\mathrm{BS}} = R_0 * P_{\mathrm{dyn}}^{-1/\epsilon}. \tag{10}$$

### 3.1.3. Chao et al. (2002) Parametric Model

Chao et al. (2002) also developed an empirical model of the shape of the bow shock based on 1,438 identified bow shocks from the magnetic field data of the Geotail mission and solar wind data from the Wind spacecraft. The functional form of the model is based off that of Shue et al. (1997) developed for the magnetopause, parameterized as

$$r = r_0 \left( \frac{1+\epsilon}{1+\epsilon\cos\theta} \right)^{\alpha} \tag{11}$$

where $r$ and $\theta$ are aberrated polar coordinates along the ecliptic plane, $r_0$ is the standoff distance, $\alpha$ is the flaring parameter, and $\epsilon$ describes the eccentricity.

The values of $r_0$ and $\alpha$ are dependent on four solar wind parameters: IMF $B_z$, $\beta$, $M_{ms}$, and $P_{\mathrm{dyn}}$. Chao et al. (2002) assumed a functional form that is bifurcated at $B_z = 0$ nT, where a two sets of fitting coefficients described $r_0$ and $\alpha$ for positive and negative $B_z$. For $B_z \geq 0$,

$$r_0 = a_1 \left(1 + a_2 B_z\right)\left(1 + a_9\beta\right)\left(1 + a_4 \frac{(a_8 - 1)M_{ms}^2 + 2}{(a_8 + 1)M_{ms}^2}\right) P_{dyn}^{-1/a_{11}} \tag{12}$$

$$\alpha = a_5 \left(1 + a_{13} B_z\right)\left(1 + a_7 P_{dyn}\right)\left(1 + a_{10}\ln(1+\beta)\right)\left(1 + a_{14} M_{ms}\right) \tag{13}$$

and similarly for $B_z < 0$,

$$r_0 = a_1 \left(1 + a_3 B_z\right)\left(1 + a_9\beta\right)\left(1 + a_4 \frac{(a_8 - 1)M_{ms}^2 + 2}{(a_8 + 1)M_{ms}^2}\right) P_{dyn}^{-1/a_{11}} \tag{14}$$

$$\alpha = a_5 \left(1 + a_6 B_z\right)\left(1 + a_7 P_{dyn}\right)\left(1 + a_{10}\ln(1+\beta)\right)\left(1 + a_{14} M_{ms}\right) \tag{15}$$

where $a_{1\text{–}14}$ are fitting parameters and $a_{12}$ is equivalent to $\epsilon$. Chao et al. (2002) determined the best-fit parameters via $\chi^2$ optimization using observed bow shocks in aberrated GSM coordinates.

### 3.1.4. Yeakel et al. (2025) Ensemble Model

Yeakel et al. (2025, hereafter Y25) leveraged a Monte Carlo approach to simulate the bow shock location for 1,000 random solar wind conditions and develop statistical bounds for the three-dimensional shape of the bow shock. The solar wind driving conditions were randomly drawn from 27 years of OMNI data (1995–2021) at 1-min resolution, with the resulting randomized subset exhibiting similar probability density functions to the full OMNI data set. The Chapman and Cairns (2003) and Jeřáb et al. (2005) parametric bow shock models were then simulated for each randomized solar wind sample, and the resulting simulations were aggregated for each base model type using a ray tracing approach. The ray tracing distances were then used to produce a mean, median, 75%, 90%, 95%, and 99% quantiles for the bow shock location in three dimensions. For more information, we refer the reader to Yeakel et al. (2025).

We used these surfaces to compare the distances of our observed bow shocks to the most probable bow shock boundary location given historical solar wind conditions. In this analysis, we compared our results to the Y25 aggregate surface of the Chapman and Cairns (2003) model assuming $\theta_{\mathrm{IMF}} = 45°$.

### 3.2. Correlation Between Bow Shock Distance and Solar Wind Parameters

First, we compared the locations of our observed bow shocks to those from the ensemble of the most statistically likely Chapman and Cairns (2003) bow shock model locations from Y25. We analyzed these relationships to inform how and which parameters are important as inputs to bow shock models. There are caveats to our analysis. Though the observed bow shock distance and the bow shock models consider the effects of multiple parameters together, we only analyze how the difference in bow shock location changes for each solar wind parameter separately. We are limited to the solar wind conditions and orbital constraints of MMS. However, our analysis can still provide insight on the dependence of the relative modeled and observed bow shock distance for different solar wind conditions.

Row a of Figure 3 shows the histogram of bow shocks and their distance from the median Y25 ensemble model, where negative (positive) is toward (away from) Earth. For every bow shock type considered, the distance of the observed bow shocks was closer to Earth by $\sim 1\ R_E$ than the median of the ensemble model, suggesting that the Chapman and Cairns (2003) model tends to overpredict the bow shock boundary from Earth. The median model distance between IMF North and IMF South bow shocks types is relatively similar. However, there is a difference in median model distance of 0.39 $R_E$ for QPerp and QPara bow shocks, where QPara bow shocks tend to be closer to Earth than predicted in the ensemble median model than that of QPerp bow shocks.

Each odd-numbered column of Figure 3 displays how the distance changes with varying solar wind parameters for a different type of bow shock described in Section 2.1. To quantify the correlation between each solar wind parameter and model distance, we calculated the Spearman rank correlation coefficient $\rho$ using the individual observations within each bow shock type, where $-1 \leq \rho \leq 1$. The closer $|\rho|$ is to 1, the stronger the monotonic relationship is between the solar wind parameter and distance. If the p-value of the correlation is significant ($\leq$0.05), we show the calculated $\rho$ for distance and solar wind parameter at the top corner of the panel (rows b–h for each odd-numbered column of Figure 3).

For each bow shock type, the most significant correlation between distance and solar wind parameter is for dynamic pressure $P_{\mathrm{dyn}}$ (Figure 3 row d), where a larger value of $P_{\mathrm{dyn}}$ pushes the bow shock surface closer to Earth. Similarly, the correlation is also strong for $n_p$, which drives the values of $P_{\mathrm{dyn}}$. The $n_p$ correlation is stronger for IMF North ($\rho = -0.646$) than IMF South ($\rho = -0.599$) bow shocks and for QPerp ($\rho = -0.687$) than QPara ($\rho = -0.613$) bow shocks. We found a mild correlation for $\beta$, $M_A$, and $M_{ms}$, where higher values of these solar wind parameters are observed for bow shocks that are closer to Earth. The model distances of IMF South and QPara bow shock types are more correlated with $\beta$, $M_A$, and $M_{ms}$ than those of IMF North and QPerp, respectively. The relationship for $v_{SW}$ and $B_{z,GSM}$ is insignificant (p-value >0.05) or only weakly correlated for each bow shock type.

Corresponding to the solar wind parameter for each bow shock type, we plotted a histogram of the distribution of values of the solar wind parameter as observed during the bow shock as a percent of each bow shock type (even-numbered columns of columns of Figure 3). We observed median $\beta = 1.77$, which is similar to the median value of $\beta = 1.16$ observed over 25 years by the Wind spacecraft (Wilson III et al., 2021), though our median $n_p = 5.43\ \mathrm{cm}^{-3}$ was slightly lower than the Wind median 7.61 $\mathrm{cm}^{-3}$. We compared the MMS observed distributions to the 10-min average of OMNI data from January 1995 through February 2024, plotted in cyan in Figure 3. The overall OMNI distributions of solar wind parameters were relatively similar to those observed during times around bow shocks identified in MMS for all bow shock types, though we observed more high velocity and higher density solar wind than the overall OMNI distribution. There was a slight deviation between overall OMNI values for quasi-perpendicular and quasi-parallel bow shock types (Figure 3 columns 8 and 10). In quasi-perpendicular bow shock distributions, there were more values in the high $\beta$ range (Figure 3f8) and fewer observations in the low proton density range (Figure 3c8) compared to the overall OMNI distribution. For QPara bow shocks, the solar wind velocity distribution was shifted higher (Figure 3b10). There were fewer low $\beta$ and low $M_{ms}$ observations than the overall OMNI distribution (Figures 3f10 and 3h10, respectively).

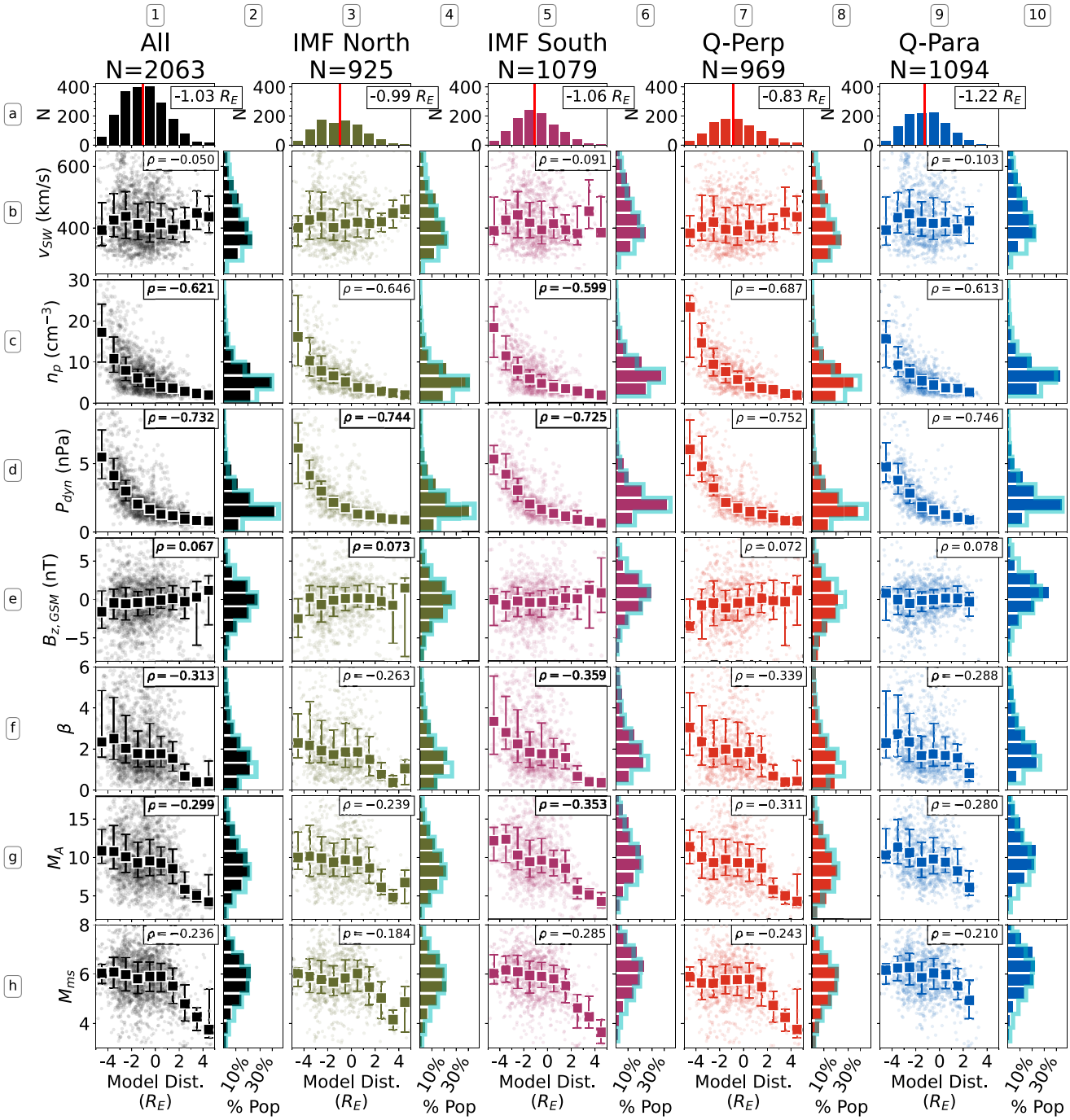


**Figure 3.** The distribution of observed and calculated OMNI upstream solar wind parameters for different types of bow shocks as a function of the difference in expected location from the Yeakel et al. (2025) median ensemble model results and the observed location of the bow shock (Rows b–h, odd-numbered columns). A negative model distance indicates that the observed location is closer to Earth than expected by the model. The square points are the median values for binned model distance and the error bar represents the interquartile range. The Spearman correlation coefficient $\rho$ is shown at the top of each panel if the correlation is significant (p−value < 0.05). The top set of histograms (row a) shows the number of bow shocks in each model distance bin. The red vertical line marks the median distance for the type of bow shock. The value of the median is shown in the top right corner of each histogram. The corresponding set of histograms on the right (even-numbered columns) shows the distribution of OMNI solar wind parameter as a function of the percent of the given bow shock type. The distribution of OMNI data at a 10-min cadence from 1995 through February 2024 is shown in cyan for reference.

### 3.3. Model Fits

#### 3.3.1. Fitting Procedure

We now fit the observed bow shocks to the parameterized model developed by Chapman et al. (2004), Jelínek et al. (2012), and Chao et al. (2002). First, we considered the effects of aberration on the bow shock location by matching the aberration correction method described for each model. The Chapman et al. (2004) and Jelínek et al. (2012), in aberrated GSE coordinates, considered only the effects of the $X$ component of the solar wind velocity while Chao et al. (2002), using aberrated GSM system, take into account the full solar wind vector. We implemented the same aberration correction for GSE and GSM coordinates.

To perform the fitting, we used the Python package `lmfit` (Newville et al., 2015), which employs a Levenberg–Marquardt least squares fitting algorithm. As initial guesses of the fitting coefficients, we adopted the best-fit coefficients reported with each model, listed in Table 1. We did not set any upper or lower bounds for the fit coefficients, which allowed them to vary over the range of real numbers. After obtaining the best-fit coefficients to our data, `lmfit` provided a $1\sigma$ uncertainty on the coefficient, which we report with the best-fit results. The uncertainty reported was the value equivalent to increasing the $\chi^2$ value of the fit by 1.

The least-squares optimization attempts to minimize the distance between the observed location of a bow shock and the model predicted location. Since MMS spends variable amount of time in different spatial regions, we utilized a weighting factor based on the amount of time MMS observed in each spatial region to properly weight each bow shock position relative to the amount of MMS observing time. For each bow shock position at location $x$, $y$, $z$, the weight applied to that position was equal to

$$w(x,y,z) = \eta * \frac{T_{total}}{T(x,y,z)} \tag{16}$$

where $T_{total}$ is the total amount of observing time of MMS on Earth's dayside and $T(x,y,z)$ is the amount of observing time within a 1 $R_E{}^3$ cube that encompasses the bow shock's position. $\eta$ is the weight normalization factor dependent on the particular bow shock type considered (e.g., all, IMF North, IMF South, QPerp, or QPara bow shocks). We calculated $\eta = \sum_{N_{BS}} \frac{T_{(x,y,z)}}{T_{total}}$, where the summation is over all bow shocks of that particular type. In practice, we considered the number of plasma regions in the T24 data set of dayside plasma regions labels for MMS1 and binned by values of 1 $R_E$ in X, Y, and Z. Since the T24 data set was at a time resolution of 1 min, $T_{total}$ was calculated as the total number of rows of MMS1 observations ($T_{total} = 999,812$ min) and $T(x,y,z)$ was the number of labeled plasma regions within the X-Y-Z spatial bin. In `lmfit`, weights are a multiplicative factor in the minimization function. X-Y-Z bins where MMS spent more time observing carried lower weight than bins less observed, so if a bow shock was observed in a spatial bin with fewer observations, it yielded greater influence on the model fit.

Due to our data constraints, we chose to simplify the fitting procedure for the Chao et al. (2002) model. After an initial fit, we found that the $a_8$ fitting coefficient, describing the dependence of bow shock position on $M_{ms}^2$ (see Section 3.1.3), was not well constrained. Therefore, we kept $a_8$ constant, adopting the best-fit value obtained in Chao et al. (2002), and performed the least-squares optimization for the remaining free parameters.

#### 3.3.2. Fit to All Bow Shocks

Table 1 lists the results of our fitting algorithm. For each model, we also list fitting diagnostics of mean absolute error (MAE), mean squared error (MSE), and the coefficient of determination ($R^2$ score) for each model fit. The MSE adds a higher penalty to outliers, so it was more sensitive to observations that do not fit the model. MAE can capture any skewness or tail in the underlying distribution. MAE and MSE provided independent evaluation to the goodness of the model fit, where a lower number indicated a better fit of the model to data. The $R^2$ score, ranging between 0 and 1 where 1 is a perfect fit, was a metric of how well the model described the underlying data. These metrics were weighted by a factor of the observing time also used to weight the model fit as described in Section 3.3.1. We also calculated the bow shock standoff distance for each model based on the mean solar wind parameters for each bow shock type, listed in Table 1.

**Table 1**
*Model Fitting Metrics, the Best-Fit Coefficients, and Bow Shock Standoff Distance for the Chapman et al. (2004), Jelínek et al. (2012) and Chao et al. (2002) Bow Shock Models*

| | Initial | All | Northward IMF | Southward IMF | QPerp | QPara |
|---|---|---|---|---|---|---|
| Chapman et al. (2004) Model Fit | | | | | | |
| MAE | 1.820 | 1.157 | 1.206 | 1.109 | 1.259 | 1.043 |
| MSE | 5.106 | 2.521 | 2.717 | 2.305 | 3.033 | 1.901 |
| $R^2$ Score | 0.752 | 0.878 | 0.864 | 0.891 | 0.871 | 0.895 |
| $J$ | 14.510 | 12.980 ± 0.060 | 12.899 ± 0.093 | 13.062 ± 0.080 | 13.219 ± 0.105 | 12.718 ± 0.108 |
| $K$ | 27.070 | 27.008 ± 1.218 | 27.035 ± 2.466 | 26.914 ± 1.321 | 25.647 ± 1.382 | 37.527 ± 4.929 |
| $A$ | 25.440 | 24.697 ± 0.105 | 24.829 ± 0.189 | 24.542 ± 0.120 | 25.226 ± 0.154 | 24.251 ± 0.166 |
| $B$ | 67.000 | 33.832 ± 4.725 | 43.470 ± 9.866 | 29.559 ± 4.803 | 29.819 ± 5.544 | 32.625 ± 9.330 |
| $a_s$ ($R_E$) | 14.132 | 12.666 | 12.521 | 12.804 | 12.775 | 12.601 |
| Jelínek et al. (2012) Model Fit | | | | | | |
| MAE | 1.562 | 1.279 | 1.294 | 1.289 | 1.538 | 1.024 |
| MSE | 4.371 | 3.369 | 3.393 | 3.324 | 4.666 | 1.775 |
| $R^2$ Score | 0.788 | 0.836 | 0.830 | 0.842 | 0.801 | 0.902 |
| $\epsilon$ | 6.550 | 6.675 ± 0.173 | 7.370 ± 0.327 | 6.344 ± 0.209 | 6.285 ± 0.228 | 7.493 ± 0.257 |
| $R_0$ | 15.020 | 15.129 ± 0.073 | 14.792 ± 0.107 | 15.411 ± 0.102 | 15.887 ± 0.133 | 14.658 ± 0.074 |
| $\lambda$ | 1.000 | 1.099 ± 0.008 | 1.072 ± 0.011 | 1.124 ± 0.011 | 1.130 ± 0.014 | 1.096 ± 0.008 |
| $R_{BS}$ ($R_E$) | 13.124 | 13.253 | 13.065 | 13.466 | 13.663 | 13.133 |
| Chao et al. (2002) Model Fit | | | | | | |
| MAE | 1.141 | 0.986 | 1.032 | 0.923 | 1.100 | 0.831 |
| MSE | 2.637 | 1.881 | 1.945 | 1.698 | 2.296 | 1.319 |
| $R^2$ Score | 0.805 | 0.861 | 0.872 | 0.861 | 0.825 | 0.903 |
| $a_1$ | 11.127 | 9.180 ± 0.179 | 9.821 ± 0.329 | 10.733 ± 0.327 | 9.930 ± 0.270 | 16.114 ± 0.777 |
| $a_2$ | 0.001 | 0.004 ± 0.000 | 0.008 ± 0.001 | −0.001 ± 0.001 | 0.004 ± 0.001 | 0.002 ± 0.001 |
| $a_4$ | 2.597 | 4.258 ± 0.187 | 3.511 ± 0.312 | 2.790 ± 0.254 | 3.776 ± 0.224 | −0.363 ± 0.290 |
| $a_5$ | 0.818 | 0.750 ± 0.091 | 0.904 ± 0.195 | 1.046 ± 0.264 | 0.451 ± 0.066 | 1.026 ± 0.134 |
| $a_7$ | −0.012 | 0.027 ± 0.006 | 0.041 ± 0.010 | 0.047 ± 0.012 | 0.029 ± 0.009 | 0.013 ± 0.012 |
| $a_8^*$ | 1.301 | 1.301 | 1.301 | 1.301 | 1.301 | 1.301 |
| $a_9$ | −0.005 | −0.000 ± 0.001 | 0.000 ± 0.001 | −0.001 ± 0.001 | −0.001 ± 0.001 | −0.002 ± 0.001 |
| $a_{10}$ | −0.033 | 0.013 ± 0.017 | −0.016 ± 0.021 | −0.007 ± 0.025 | −0.013 ± 0.026 | 0.029 ± 0.024 |
| $a_{11}$ | 6.047 | 6.974 ± 0.195 | 6.529 ± 0.287 | 6.307 ± 0.268 | 7.249 ± 0.296 | 6.033 ± 0.226 |
| $a_{12}$ | 1.029 | 0.737 ± 0.115 | 0.517 ± 0.150 | 0.498 ± 0.150 | 1.164 ± 0.232 | 0.872 ± 0.145 |
| $a_{13}$ | 0.023 | −0.007 ± 0.002 | −0.014 ± 0.002 | 0.007 ± 0.004 | −0.010 ± 0.002 | 0.003 ± 0.004 |
| $a_{14}$ | −0.002 | 0.031 ± 0.010 | 0.066 ± 0.018 | 0.015 ± 0.013 | 0.063 ± 0.022 | −0.034 ± 0.008 |
| $r_0$ ($R_E$) | 13.325 | 13.451 | 13.203 | 13.414 | 13.895 | 13.207 |

*Note.* Fit coefficients marked with * were kept constant during the fit. We calculated standoff distances using the mean solar wind values for each bow shock type. The mean values $(\overline{P_{dyn}}, \overline{B_z}, \overline{\beta}, \overline{M_A}, \overline{M_{ms}})$ were (2.42 nPa, −0.35 nT, 3.02, 10.57, 5.77) for all, (2.50 nPa, −0.53 nT, 3.21, 10.61, 5.71), for IMF North, (2.35 nPa, −0.19 nT, 2.85, 10.53, 5.81), for IMF South, (2.58 nPa, −0.73 nT, 2.95, 9.95, 5.48), for QPerp, and (2.288 nPa, −0.01 nT, 3.08, 11.12, 6.02) for QPara bow shock types.

When we inputted our observations into the initial parameters provided by Chapman et al. (2004), Jelínek et al. (2012), and Chao et al. (2002), we found that the best literature model was the Chao et al. (2002) parametrization in terms of MAE, MSE, and $R^2$ score. The Chapman et al. (2004) yielded the worst performance overall, with the lowest initial $R^2$ score and highest MAE and MSE.

We performed the least-squares fit on the entire catalog of bow shocks that we identified with MMS1 (see Section 2.1). The best performing model for all bow shocks was the Chapman et al. (2004) with an $R^2$ score of 0.878, with Chao et al. (2002) and Jelínek et al. (2012) second and third best performing with $R^2$ scores of 0.861 and 0.836, respectively. However, the high $R^2$ score of all three models indicated a reasonable fit.

The models with the updated parameters are shown compared to each model's initial parameters in Figure 4. We note that the Chapman et al. (2004) and Jelínek et al. (2012) fits are shown in GSE coordinates while the Chao et al. (2002) fit is in GSM coordinates. The plotted surfaces were assuming a set value for the input solar wind parameters. We used the mean value of the solar wind parameter for the entire bow shock catalog, listed in Table 1.

Figures 4a–4c compares the initial and best-fit parameters of the Chapman et al. (2004) model. In our fitting, we found that the best fit pulls inward the standoff distance, dependent on parameters $J$ and $K$ in Table 1. In other words, the standoff distance of all bow shocks was closer to Earth than what Chapman et al. (2004) predicted by 1.5 $R_E$. The largest changes between initial parameters from Chapman et al. (2004) and our best fit results was in the fit coefficient $B$. We obtained a much lower value of $B$, which indicates lower dependence on the $1/M_A^2$ parameter in the terminator distance and suggests that the shock is found to be statistically more broad and with a larger opening angle compared to the results in Chapman et al. (2004). However, we note the relatively large uncertainty associated with $B$, indicating that the best-fit value was not as well constrained.

Figures 4d–4f show the results of the Jelínek et al. (2012) model fit. Our best-fit parameters were very similar to that reported by Jelínek et al. (2012), as was the calculated standoff distance. This may be due to the similarity in the underlying bow shocks observed by MMS and by THEMIS implemented in the Jelínek et al. (2012) study, both in the time in the solar cycle and their position mostly on the equatorial plane. However, there is a visual difference in the initial and best-fit model which indicates that the best-fit shape is less flared at the flanks than reported in Jelínek et al. (2012).

The best fit for the Chao et al. (2002) bow shock model was similar to those of the initial parameters, as shown in Figures 4g–4i. In the fit coefficients that control the standoff distance, the most significant differences in the best-fit value from the initial value was in $a_1$, where our fit value is lower than that of Chao et al. (2002), and higher value for $a_{11}$, the power law quantity dependent on $P_{\mathrm{dyn}}$, which would indicate a steeper relationship. This indicates that our model is more tuned to the effect of dynamic pressure on standoff distance. We also found that the best-fit $a_4$ parameter was higher, indicating a stronger dependence on $M_{ms}$. Best-fit values for coefficients $a_2$ and $a_9$ were also different but both initial and best-fit values were small, so a change in these coefficients would not contribute drastically to a change in bow shock shape.

In the flaring parameter, the biggest discrepancy was in $a_{13}$ and $a_{10}$. The best-fit value of $a_{13}$ was much lower than the initial value, which would indicate a lower dependence on $B_z$ than presented in Chao et al. (2002). The best-fit value of $a_{10}$, the coefficient in front of $\ln(1 + \beta)$, was lower by a factor of $\sim$2 than initial values, which would mean a more negative correlation with $\beta$. We also found a significant difference in the eccentricity parameter ($a_{12}$). For the overall sample, we found an eccentricity parameter $\sim$3 times lower than the Chao et al. (2002) value. However, we note from Figures 4g–4i that the initial and best-fit model shapes were extremely similar to each other. Though the eccentricity parameter was different between these two fits, the overall shape was not affected by the different eccentricity. The standoff distance calculated with initial and updated model parameters was also similar.

Figures 4i–4l compares the Chapman et al. (2004) and Jelínek et al. (2012) models after our fitting procedure. We did not include the Chao et al. (2002) in this comparison because of the difference in coordinate systems. The best-fit Chapman et al. (2004) and Jelínek et al. (2012) functional forms were extremely similar to each other as cross sections on all planes. The overall best-fit standoff distance is $\sim$13 $R_E$ for all bow shocks, with the Chapman et al. (2004) model producing the closest standoff and Chao et al. (2002) with the furthest.

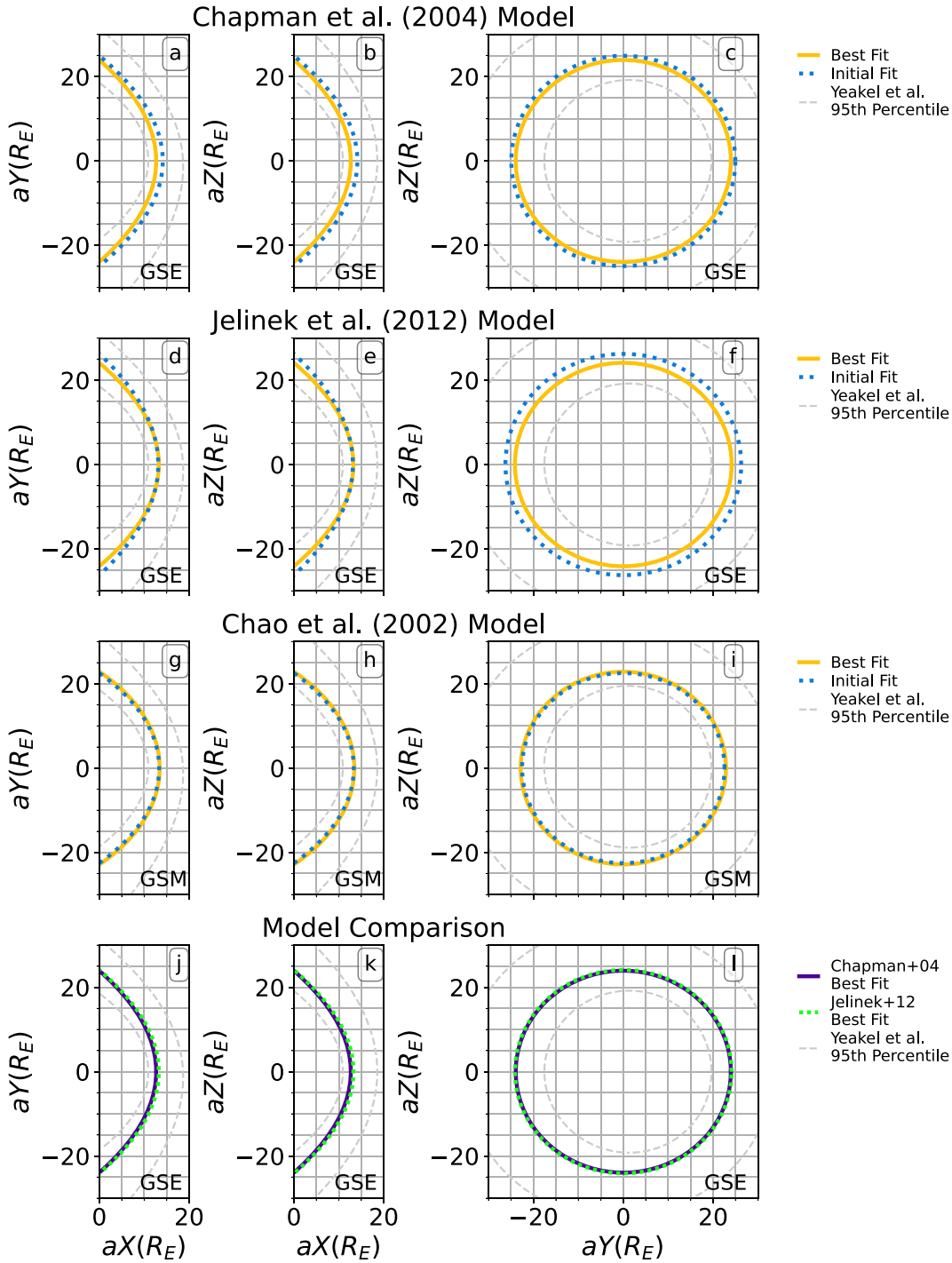


**Figure 4.** The Chapman et al. (2004), Jelínek et al. (2012), and Chao et al. (2002) models fit to the entire bow shock catalog. The models with updated fitting parameters from this work listed in Table 1 are shown as solid lines. The models with initial parameters are plotted as dotted lines. We compare the Chapman et al. (2004) and Jelínek et al. (2012) updated bow shock models in the last row. The 95% quantile boundaries from the Y25 ensemble model, corrected for an average 4° aberration, is shown as the dashed line for reference. The fits and bow shock types are shown in aberrated GSE and GSM coordinate systems.

#### 3.3.3. Fit to Northward and Southward IMF Bow Shocks

When the IMF is southward $(B_z < 0)$, magnetic reconnection can occur at the dayside magnetopause (Dungey, 1961). This process transfers magnetic flux to the tail, which, through pressure balance, may drive the magnetopause closer to Earth (Holzer & Slavin, 1978). Such motion also alters the bow shock location and its modeling efforts, affecting models that use the magnetopause standoff distance to parameterize shock position. Moreover, statistical studies show that under southward IMF the magnetopause standoff distance depends on the magnetic field magnitude than it does under northward IMF (Shue et al., 2011).

Accordingly, we analyze bow shock subsets with northward ($\theta_{cl} \geq 0°$) and southward IMF ($\theta_{cl} < 0°$) to evaluate any differences. We fitted the models to the IMF North bow shocks and IMF South bow shocks separately. The best-fit coefficients are listed in Table 1, as well as the full suite of performance metrics and calculated standoff distances for each model. For bow shocks with Northward IMF, all three models yielded relatively similar goodness of fit results. The model with the highest resulting $R^2$ score (0.872) was the Chao et al. (2002) model whereas the Jelínek et al. (2012) model had the lowest (0.830). The Chapman et al. (2004) model was the best performing model for Southward IMF bow shocks $(R^2 = 0.891)$ while the Jelínek et al. (2012) model was the worst performing in $R^2$ (0.842) score.

In Figure 5, we show the models plotted with the best-fit parameters for Northward IMF and Southward IMF bow shocks. When comparing the best-fit parameters between the northward and southward IMF bow shocks, most parameters between the two types were very similar, though we observed a few significant differences. The parameter $B$ in the Chapman et al. (2004) model was $\sim$1.5 times higher in northward IMF fit than it is in the southward IMF. This could indicate that northward IMF bow shocks were much more dependent on the value of $M_A$ than the southward IMF bow shocks, though we do note the large uncertainty associated with the best-fit values of $B$. In the best-fit Jelínek et al. (2012) model, the fit for the Northward IMF had a higher $\epsilon$ value than that of the Southward IMF bow shocks, indicating a steeper power law to $P_{\mathrm{dyn}}$. The difference in standoff distance between IMF North and IMF South was also largest in the Jelínek et al. (2012) model, though the difference was not significant in any of the models considered. In the Chao et al. (2002) model, the eccentricity parameter $a_{12}$ was much higher for Northward IMF bow shocks than for Southward IMF bow shocks. The Chao et al. (2002) model shows the largest visual difference between the Northward IMF and Southward IMF fits (Figure 5i).

The definition of the IMF North and IMF South bow shock type introduced in Section 2.2 uses a strict mathematical cuttoff of $\theta_{cl} = 0°$. However, variability in the IMF can introduce uncertainties when averaging over several minutes to obtain upstream and downstream parameters. Thus, we also considered a less stringent definition using only bow shocks with $\theta_{cl} \geq 30°$ as IMF North and $\theta_{cl} \leq -30°$ as IMF South and refit the Chapman et al. (2004), Jelínek et al. (2012), and Chao et al. (2002) models based on this definition. We do not find any significant variation (>10%) in the model fit parameters after fitting the IMF North and South population using the $|\theta_{cl}| \geq 30°$ definition. Therefore, while there may be IMF variability inherent to our calculations, these variations are not affecting the IMF North and IMF South bow shock behavior or model in our analysis.

#### 3.3.4. Fit to Quasi-Perpendicular and Quasi-Parallel Bow Shocks

We also performed separate fits for quasi-perpendicular bow shocks and quasi-parallel bow shocks. We list the resulting best-fit parameters and metrics in Table 1 and compare the model shapes in Figure 6. The model that best described the QPerp bow shocks was the Chapman et al. (2004) model $(R^2 = 0.871)$ while the Chao et al. (2002) model was the best performing for quasi-parallel bow shocks $(R^2 = 0.903)$. All models yielded better performance on the best-fit values for quasi-parallel bow shocks than QPerp bow shocks. In the Chapman et al. (2004) model, the best fit for quasi-parallel bow shocks had higher $K$ and $B$ coefficients than the best fit for quasi-perpendicular bow shocks. Both $K$ and $B$ control the relationship with $M_A$, which could indicate that quasi-parallel bow shock location was more sensitive to $M_A$ than quasi-perpendicular bow shocks. All three models indicated the standoff distance was closer to Earth for QPerp bow shocks than for QPara. The standoff distance $R_{BS}$ in the Jelínek et al. (2012) model was 0.53 $R_E$ further for QPerp than for QPara bow shocks, which was consistent with the observed distribution of QPerp versus QPara bow shocks model distance (Figures 3a7 and 3a9). In the Chao et al. (2002) best fit the difference was 0.69 $R_E$ between quasi-perpendicular and quasi-parallel model standoff. Fit parameter $a_1$ was much higher but $a_4$ was much lower in the parameters when comparing the

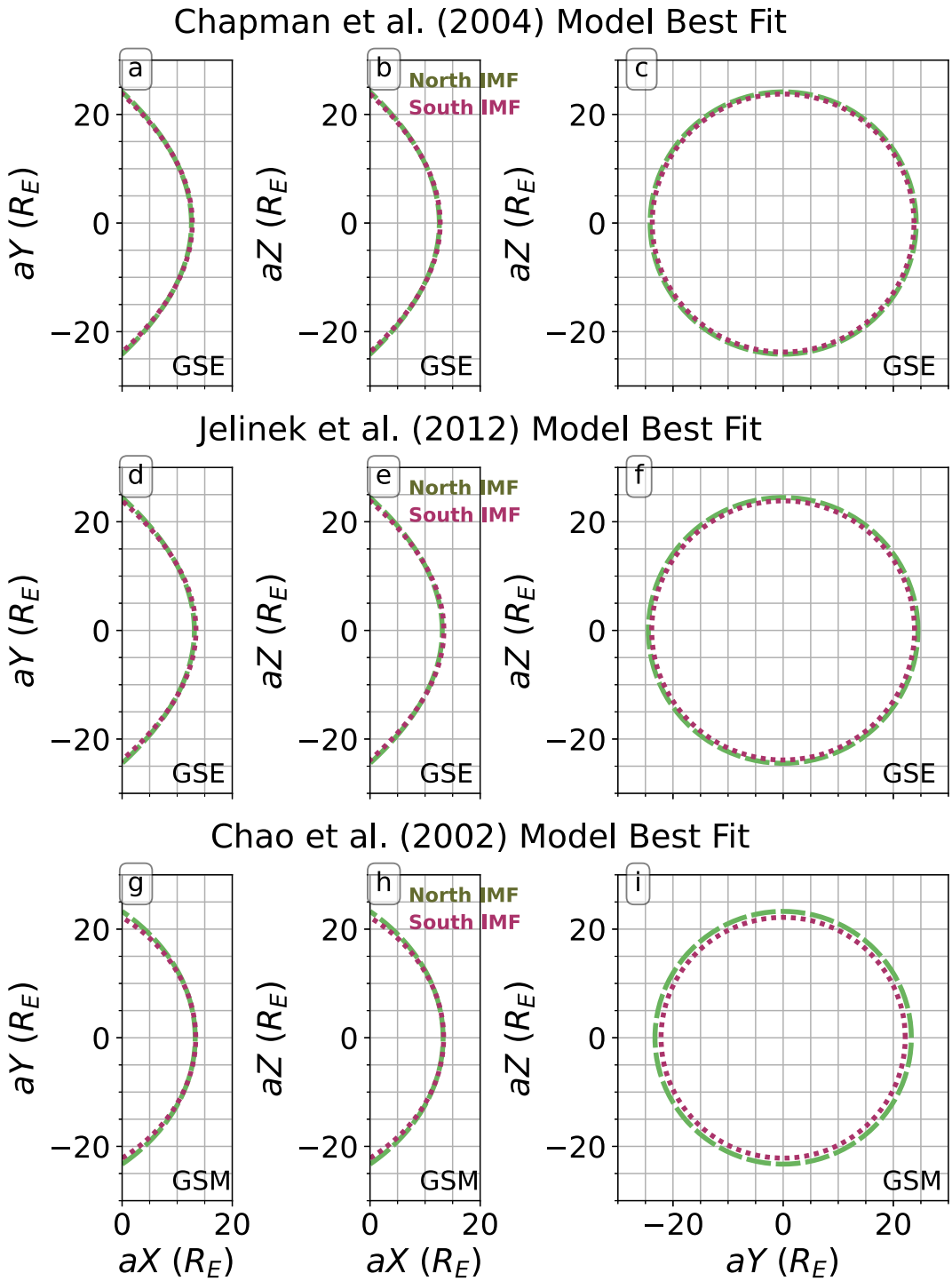


**Figure 5.** The best-fit Chapman et al. (2004, panels a–c), Jelínek et al. (2012, panels d–f), and Chao et al. (2002, panels g–i) models for the Northward IMF (green) and Southward IMF (magenta) bow shock types, shown in the aberrated coordinate system denoted at the bottom right of each panel.

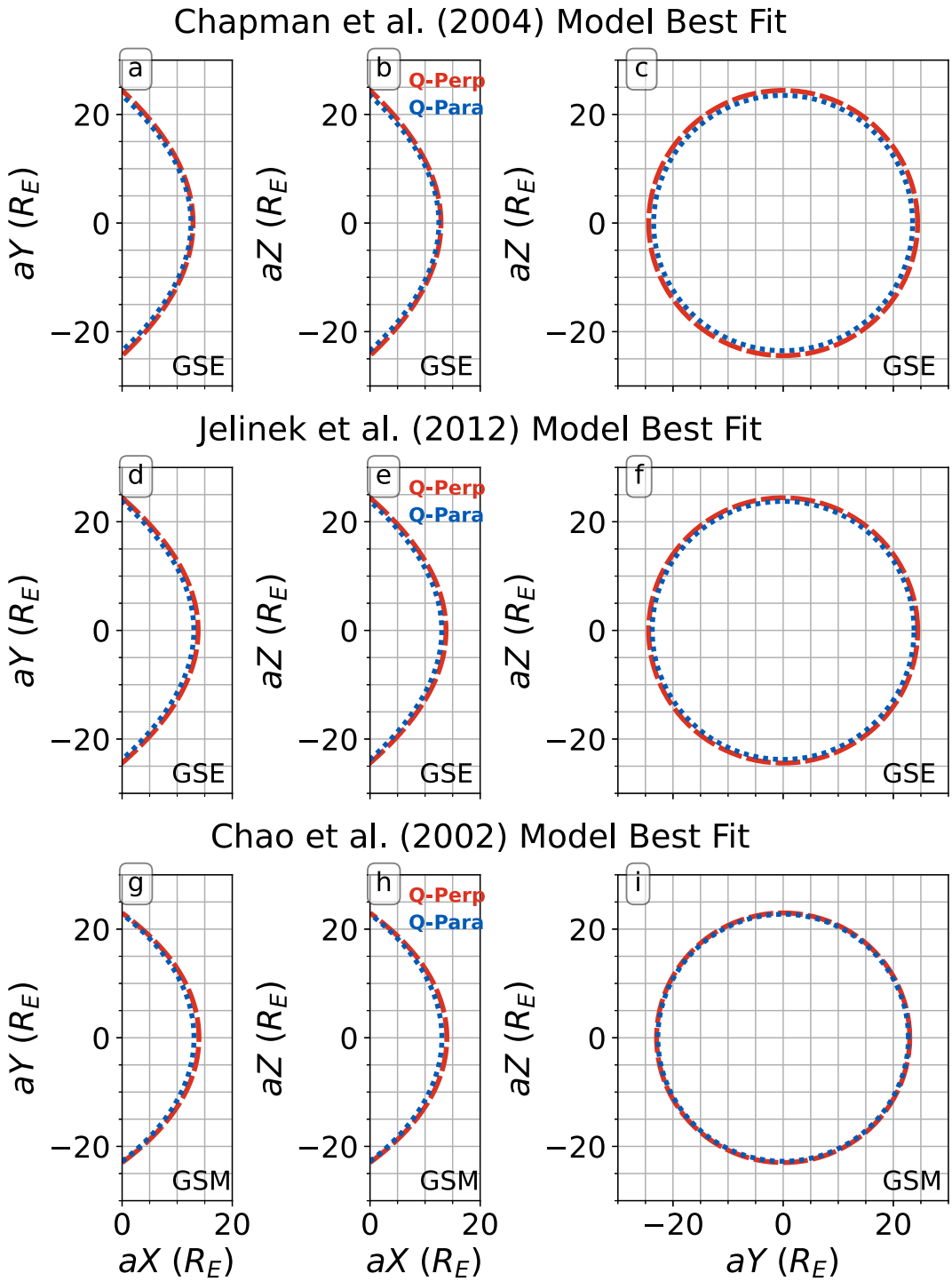


**Figure 6.** Same as Figure 5 except comparing the quasi-perpendicular (red) and quasi-parallel (blue) bow shock types for best-fit Chapman et al. (2004, panels a–c), Jelinek et al. (2012, panels d–f), and Chao et al. (2002, panels g–i) models.

parameters that constituted these standoff distance calculations, indicating that the standoff distance for QPerp has a stronger dependence on $M_{ms}$ than QPara.

In Figure 6, we can observe the difference between the QPara and QPerp bow shock stand off distance in the Jelínek et al. (2012) and Chao et al. (2002) models. We discerned that the flaring of the paraboloid shape was more

pronounced for QPerp bow shocks than it was for QPara in the Chapman et al. (2004) model, where the best-fit Qpara model is more inward than that of the QPerp toward the flanks.

### 3.4. Comparison of Observed and Model Predicted Locations

We compared the model distance (i.e., the difference between the observed and model predicted location) to evaluate how our updated models are describing the observed data. We calculated the predicted location for each model using our best-fit model parameters listed in Table 1 with the observed solar wind conditions observed at each bow shock. With this definition, a negative model distance indicates that the observed location is closer to Earth than expected by the model.

Figure 7 shows the relationship between solar wind conditions and model distance for each model, where black points are those from the population of all bow shocks and black squares are median values within each model distance bin. Row a of Figure 7 shows the model distance distribution. We find that the median and standard deviation of the model distance distribution is $-0.16 \pm 1.57$, $-0.49 \pm 1.77$, and $-0.35 \pm 1.40$ for the Chapman et al. (2004), Jelínek et al. (2012), and Chao et al. (2002) models, respectively, meaning the best-fit models can predict bow shock locations relatively well, but have a wide spread.

However, there are still discrepancies in observed and modeled bow shock locations. We find that the model distance for the best-fit Chapman et al. (2004) model (Figure 7 column 1) underpredicts the bow shock location for high dynamic pressure and overpredicts at low pressure (Figure 7d1), even though the Chapman et al. (2004) functional form includes $P_{\mathrm{dyn}}$. The Spearman correlation coefficient, calculated using the individual observations of each bow shock, between model distance and $P_{\mathrm{dyn}}$ is $\rho = 0.184$, indicating a slight positive correlation. A similar relationship is present for solar wind speeds (Figure 7b1). For other solar wind parameters $n_p$, $B_{\mathrm{z,GSM}}$, $\beta$, $M_A$, and $M_{ms}$, there is not a strong or significant correlation of the solar wind parameter with model distance.

As shown in Figure 7d2, the Jelínek et al. (2012) best-fit model distance is not significantly correlated with $P_{\mathrm{dyn}}$, though we do observe an increase in model distance with $v_{\mathrm{SW}}$ (Figure 7b2, $\rho = 0.195$). However, shown in Figures 7f2, 7g2, and 7h2, the best-fit Jelínek et al. (2012) model underpredicts bow shock locations with lower $\beta$ ($\rho = -0.30$), $M_A$ ($\rho = -0.28$), and $M_{ms}$ ($\rho = -0.24$). While none of these parameters are contained in the model's functional form, they still have significant correlations with the model distance. This suggests that large differences in model distance may still be driven by $\beta$, $M_A$, and $M_{ms}$. For the best-fit Chao et al. (2002) model (Column 3 of Figure 7), the model distance is most correlated with $v_{SW}$ ($\rho = 0.162$), $n_p$ ($\rho = -0.189$), and $P_{\mathrm{dyn}}$ ($\rho = -0.140$), though the correlation coefficients do not indicate a strong correlation.

In Figure 7, we also compared model distance to the IMP 8 bow shock catalog (Merka et al., 2003), plotted in green. The IMP 8 spacecraft observed 10,748 bow shock crossings between 1973–1981 and 1997–1999. We limited our comparison to only those (a) on the dayside ($X_{GSE} > 0$), (b) while both plasma and field observations were present, (c) identified in either field, plasma, or both data sets, and (d) where upstream solar wind conditions were steady and well defined. These restrictions limited the catalog to 133 bow shocks that matched our criteria that were observed primarily at the flanks. Despite the low numbers, the IMP 8 bow shocks offer a counterpoint to the MMS bow shock catalog in comparing how the best-fit models are performing for bow shocks observed during different solar wind conditions and locations at the bow shock.

In Column 4 of Figure 7, the IMP 8 bow shocks offer a significantly different distribution in $\beta$, $M_A$, and $M_{\mathrm{ms}}$ compared to all bow shocks in this analysis. The model distance for the three best-fit models are large, indicating that the models are not able to predict the locations of these bow shocks because the solar wind conditions are extreme compared to the bow shocks considered in the fit. However, the IMP 8 model distances extend and corroborate the correlations between solar wind parameters that were observed from the model distances calculated from MMS bow shocks at extreme solar wind conditions. For example, IMP 8 model distances for the best-fit Jelínek et al. (2012) model is still strongly negatively correlated with low $M_A$ and $M_{ms}$ (Figures 7g2 and 7h2).

The comparison of IMP 8 and MMS bow shocks highlight the orbital limitations and biases inherent in these two data sets. IMP 8 primarily observed bow shocks near the flanks closer to Earth and its orbit never reached the regions where models would predict the bow shock location during periods of low Mach numbers. In contrast, MMS bow shock crossings occur mainly near the equatorial plane around $\sim 12\ R_E$, where its dwell time is greatest

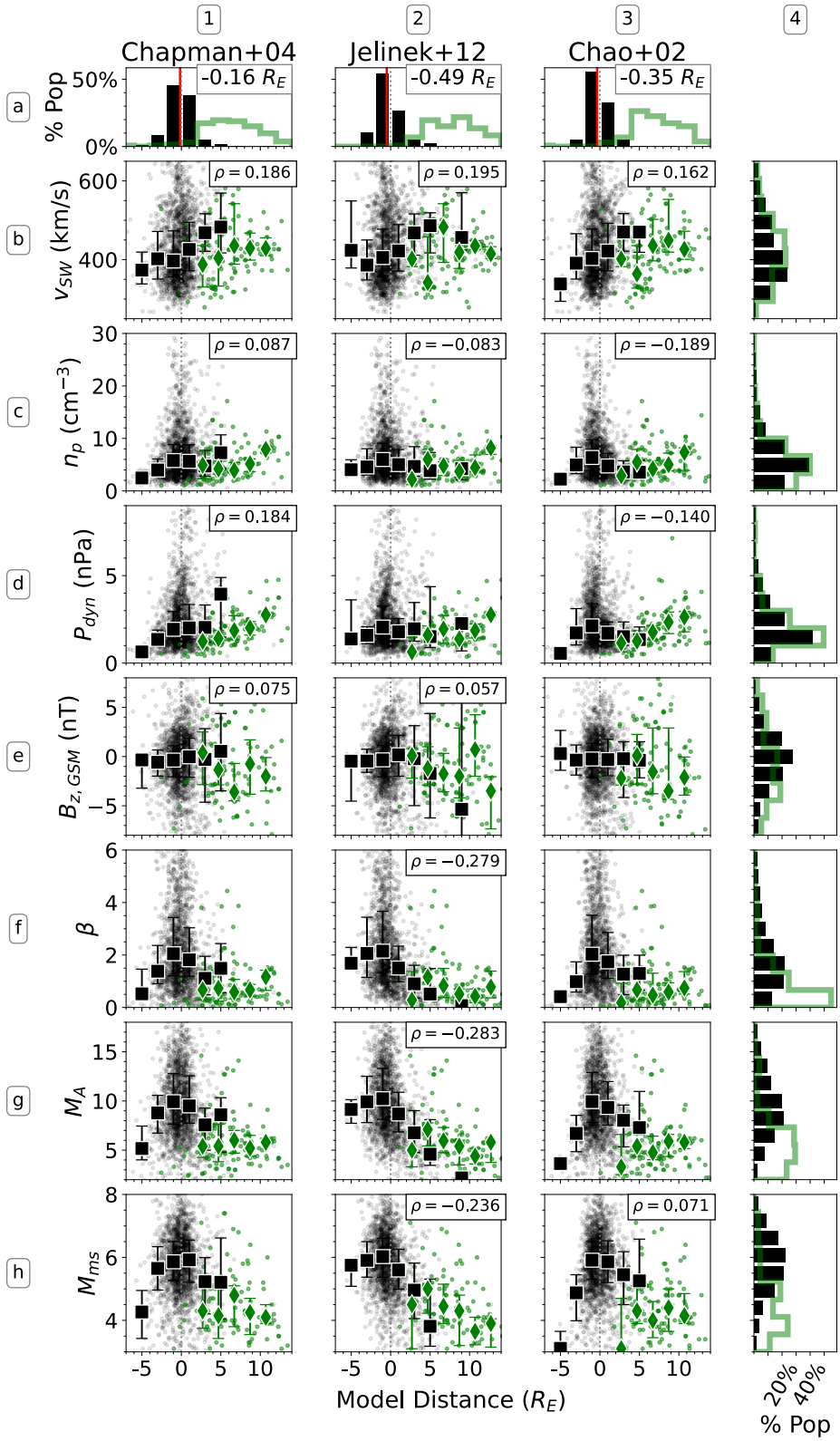


**Figure 7.**

(see Figure 2). Although models predict shock positions well beyond the observational range of MMS, the spacecraft's orbital constraints prevent robust sampling of more distant shocks, which are typically associated with low Mach numbers and low dynamic pressures. Any MMS bow shocks observed with low Mach number and low dynamic pressure most likely occurred while the bow shock was not in equilibrium position.

### 3.5. Examples of Bow Shocks at Extreme Solar Wind Conditions

We identified bow shocks that occurred at the extremes of our observed solar wind conditions and investigated their model difference using initial and updated fitting parameters in Chapman et al. (2004), Jelínek et al. (2012), and Chao et al. (2002). In Figure 8, we show the observed bow shock locations, the MMS and OMNI quantities, and the plasma region labels from T24 for four example bow shocks. The Y25 ensemble median model is shown as reference of the bow shock shape at normal solar wind conditions. The 2023 February 2 bow shock occurred close to the post-noon sector and at equatorial latitudes. The initial model distance was discrepant among the three models, where the Jelínek et al. (2012) model distance was 1.3 $R_E$ (92 percentile) while the Chapman et al. (2004) and Chao et al. (2002) models predict negative model distances of $-1.99$ $R_E$ and $-1.14$ $R_E$, respectively. We observed a sharp increase in the MMS total magnetic field and ion density and a decreased bulk velocity that is indicative of a true quasi-perpendicular bow shock around 17:21 UTC. In the concurrent OMNI data, we observed that the total magnetic field, ion density, and flow speed quantities remain consistent with those observed by MMS on the solar wind side of the bow shock. Considering the ±10-min average around the bow shock crossing, the density during the time of shock crossing was extremely low ($n = 1.8\ \mathrm{cm}^{-3}$) which drove down the dynamic pressure ($P_{dyn} = 0.4$ nPa). In Figure 7 row g, we also observed a decrease in Mach number $M_A$ with increasing model distance with Spearman correlation coefficient $\rho = -0.279$ for the model distance compared to the Jelínek et al. (2012) model. For this bow shock, the average OMNI observed value for Mach number was also relatively low ($M_A = 4.3$). In the overall 29-year sample of OMNI data available, the observed pressure and Mach number were in the lowest 1% and 4%, respectively, of all observed values, indicating an extreme solar wind condition. After updating the model fit parameters, the Jelínek et al. (2012) model distance actually became more extreme (1.8 $R_E$) while the Chapman et al. (2004) and Chao et al. (2002) model distances improved (0.22 $R_E$ and $-0.48$ $R_E$, respectively). The Jelínek et al. (2012) model does not consider the Mach number value directly, which may explain its poor performance for this bow shock.

On 2022 7 April, MMS observed four consecutive quasi-perpendicular bow shock crossings between 22:30 and 23:45 UTC. We included three of these crossings in our bow shock list. The bow shock at 22:58 UTC was excluded after grouping because it occurred within 20-min of another bow shock (see Section 2.1). These bow shocks occurred along the dawn flank. We found that the observed OMNI and MMS quantities for magnetic field and flow velocity on the solar wind side of the bow shocks were consistent. The OMNI-observed $M_A = 4.8$ and $P_{dyn} = 0.8$ nPa were low during these bow shocks (in the lowest 7th and 8th percentile, respectively) in the overall OMNI sample. The initial model distances are extreme (>90th percentile for all three models) and the model distances are larger after updated parameters (2.35 $R_E$, 3.52 $R_E$, and 2.81 $R_E$ for the Chapman et al. (2004), Jelínek et al. (2012) and Chao et al. (2002) models, respectively), which indicates that the models were still unable to well describe the bow shock during these extreme solar wind conditions.

The 2021 21 March bow shock occurred close to Earth's subsolar point. The model distance for the Chapman et al. (2004), Jelínek et al. (2012), and Chao et al. (2002) initial models was $-0.96$ $R_E$, $-0.35$ $R_E$, $-0.51$ $R_E$, respectively, typically because of high dynamic pressure as a result of dense solar wind pushing the bow shock surface inward. The MMS data showed a gradual shock transition at 12:32 UTC. The averaged solar wind density, pressure, and Mach number during the bow shock was high ($n = 21.6\ \mathrm{cm}^{-3}$, $P_{dyn} = 5.7$ nPa, $M_A = 9.8$). Indeed, the observed density and pressure were in the highest 98% and 97%, respectively, in overall observed OMNI

**Figure 7.** Comparison of the model distance (difference between observed and predicted bow shock location) versus different solar wind parameters for the Chapman et al. (2004), Jelínek et al. (2012), and Chao et al. (2002) models. We calculate location of each model using the solar wind conditions for each bow shock. A negative model distance indicates that the observed location is closer to Earth than expected by the model. The black points are those from the population of all bow shocks used in this analysis while the green are those from the IMP 8 bow shock catalog. The Spearman correlation coefficient $\rho$ for all bow shocks is displayed at the top of each panel if significant (p−value < 0.05). The black square and green diamond points are the median values for model distance bins for all and IMP 8 bow shocks, respectively, where the uncertainty represents the interquartile range. The histograms in Row a and Column 4 are the model distance and solar wind parameter distribution, respectively, where the red line indicates the median model distance.

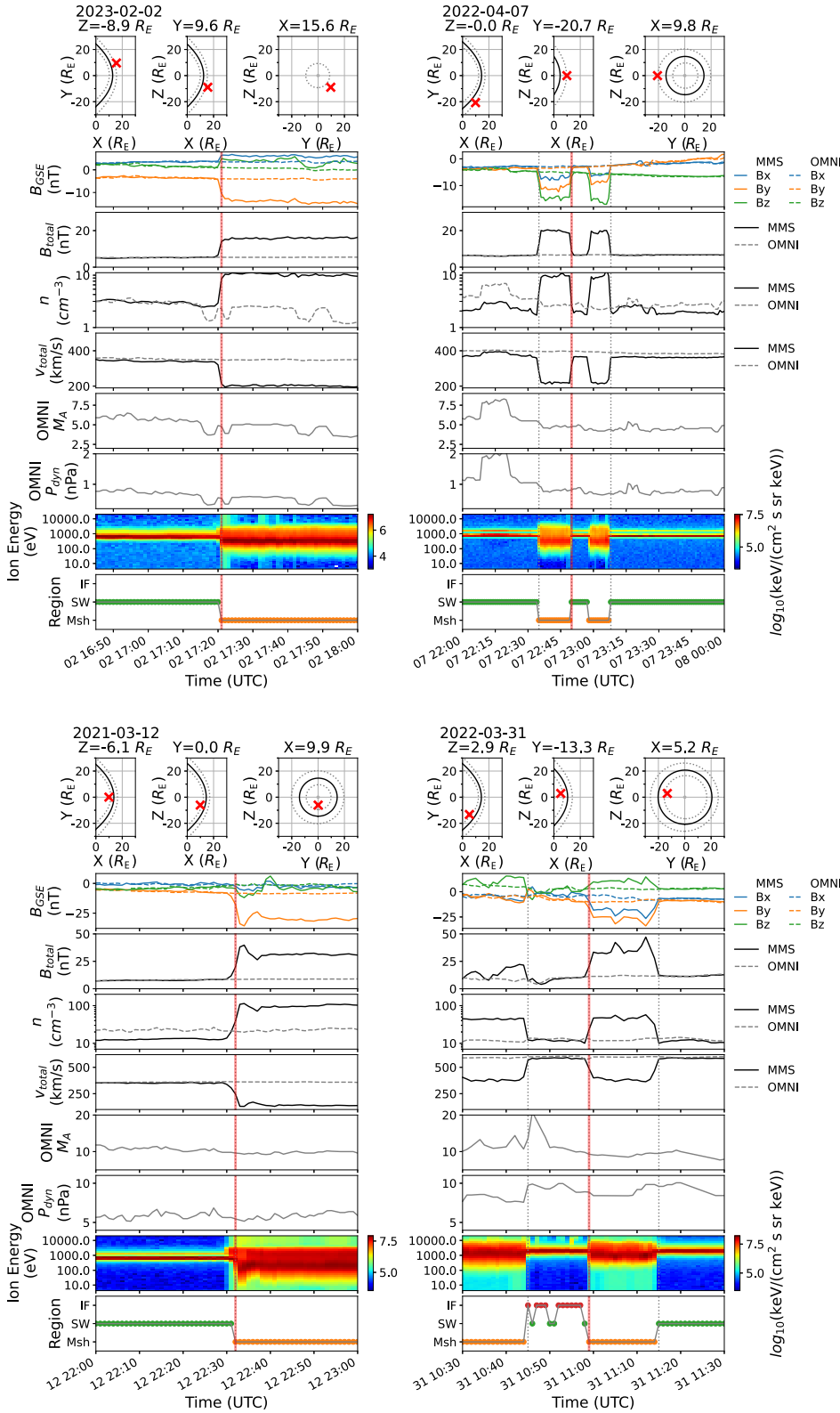


**Figure 8.** Four examples of bow shocks observed during extreme solar wind conditions. For each bow shock, the observed location (red x) and the Y25 median (black solid) and 75% confidence interval (gray dotted) model boundaries at the bow shock location are shown in the top three panels. The subsequent rows show the observed MMS and OMNI magnetic field components and magnitude, proton density, flow speed, Alfvénic Mach number, and dynamic pressure with the time of the bow shock (red solid) and any additional bow shocks (gray dashed) marked as vertical lines. The MMS ion energy spectra and the plasma region label from T24 are shown in the last two rows.

values while the observed Mach number was relatively nominal (57th percentile). After updating the model fits, the model distances improved for the Chapman et al. (2004) and Jelínek et al. (2012) models (0.29 $R_E$ and −0.33 $R_E$, respectively) but the updated model distance was shifted more Earthward for the Chao et al. (2002) model (−0.84 $R_E$).

We also show a series of quasi-parallel and quasi-perpendicular bow shock transitions crossed by MMS on 2022 31 March. These bow shocks are examples of model and observed location mismatch on Earth's dawn flank. OMNI solar wind density ($n$ = 12.3 cm$^{-3}$), Mach number ($M_A$ = 9.5) and pressure ($P_{dyn}$ = 8.7 nPa) were all high during the entire observation. Again, the density and pressure were extreme compared to observed OMNI solar wind conditions (95th and 99th percentile, respectively) while the Mach number was relatively normal (54th percentile). These examples indicate that the bow shock boundary shape was more likely to be pushed Earthward by dense, high pressure upstream solar wind, whereas Mach number was a secondary driver. While the updated model distance improved for the Jelínek et al. (2012) and Chapman et al. (2004) models, the updated Chao et al. (2002) model yielded a higher, more Earthward model distance after updating (−1.24 $R_E$) than the initial model performance (0.29 $R_E$). The Chao et al. (2002) model required more input solar wind parameters and was a more complex parametrization than the Jelínek et al. (2012) and Chapman et al. (2004) models. While the Chao et al. (2002) model had a reasonable $R^2$ in the updated fit (see Table 1, it may also be overfit to the observed solar wind conditions and are not able to well describe the bow shock during times of extreme pressure and density.

Overall, the large errors exhibited by these models under extreme conditions indicate that our current MHD and empirical-driven formulas still struggle to accurately predict the bow shock during these solar wind conditions. This implies that full physics-based simulations may be necessary to better capture the bow shock's shape and structure during such rare driving conditions.

## 4. Discussion

All three models discussed in this study provided similar performance after fitting for MMS bow shocks. This suggests that all three models can describe the bow shock shape well after updating the fit parameters to MMS observations. Though these parameters were representative of MMS data, we attempted to make the fits applicable to observations outside of MMS. Comparison to 29 years of OMNI data gives credence that MMS observations of bow shocks occur at times representative of a range of solar wind conditions (see Figure 3 and discussion in Section 3.2). Though the models with our updated fit parameters were able to better predict the locations of the majority of MMS bow shocks, we found that the updated models are still not able to well describe bow shock locations during extreme solar wind conditions. This was demonstrated with predicted locations of IMP 8 bow shocks that were observed during different solar wind conditions than that of MMS. Any potential users should be aware of the constraints of the model due to MMS observations, especially in regard to solar wind conditions, lack of high latitude bow shocks, and the peculiarities of the MMS orbit.

For the Chapman et al. (2004) model, an updated fit with MMS observed bow shocks generated a standoff distance closer in to Earth. While this could be the product of MMS orbits biasing the number of bow shocks closer into Earth, we attempt to alleviate the bias by weighting higher the bow shocks with fewer observations. However, because each study and model was based on their own unique set of observations, it introduces biases that cannot be compared across studies. Out of the three models compared, the Jelínek et al. (2012) model was most similar in approach to ours, in that they use THEMIS observations comparable to MMS and a similar weighting to their data. The standoff distance we estimated with our fits was also closest to that presented in Jelínek et al. (2012). Future work could be to include a comprehensive list of bow shocks across multiple missions in one model.

We found very little difference in the shape of northward IMF and southward IMF bow shocks. We did not observe significant differences in fit parameters for any of the models described for the fit of these two types. Furthermore, we did not observe any significant correlation between $B_z$ and model distance. Though studies show that the IMF direction may impact the standoff distance of the magnetopause (e.g., Shue et al., 2011), our results suggest that statistically speaking a separate model under these configurations (e.g., Chao et al., 2002) might not contribute significantly to a more robust modeling effort. This result also showed that the other properties that change the bow shock location and shape (e.g., $P_{\mathrm{dyn}}$ and $M_A$) were not associated with a preferential northward or southward IMF configuration. It should be noted, that further analysis may be required here as propagation errors may influence this result since for many occasions changes between northward and southward IMF may be

associated with different solar wind parcels that can have different propagation time to Earth's bow shock. Furthermore, the averaging process performed on the input data from OMNI could also affect such rotations since some of them may have been smoothed or filtered out.

We found that there was a systematic difference in the best fit for quasi-perpendicular and quasi-parallel bow shocks. Quasi-perpendicular bow shocks were typically further out from Earth than quasi-parallel bow shocks. This could originate from a variety of reasons. First, the determination of the shock location may be affected by the upstream foreshock found in quasi-parallel shocks. However, this potential systematic error is unlikely to favor a closer location to Earth over a further one as the presence of foreshock waves will, if any, introduce signatures of a shock crossing further upstream. An alternative scenario is that the presence of non-linear wave activity and shock reformation at quasi-parallel shocks (e.g., Johlander et al., 2022; Raptis et al., 2022) pushes the nominal location of the shock further inwards compared to quasi-perpendicular ones. Another alternative would be that foreshock transients with regions of localized elevated dynamic pressure (An et al., 2020; Kajdič et al., 2017) move the shock location inwards. Since such processes cannot be captured by the OMNI solar wind data, a detailed analysis associating each crossing with local in situ upstream measurements may be useful in assessing the contribution of these effects.

## 5. Summary and Conclusions

In this study, we analyzed the locations of 2,063 bow shocks observed with MMS between 2015 and 2024. The goal of this study was to compare the observed locations of the bow shocks to those predicted by literature parametric models and determine how well these shape models can describe the observed location given a range of solar wind conditions.

The distribution of solar wind parameters observed during the MMS bow shock sample was in good agreement with the overall distribution of the solar wind conditions over the past 30 years from OMNI (see Figure 3). Deviations between the median bow shock shape and observed bow shocks are largely driven by the dynamic pressure $P_{dyn}$ and correlated with the solar wind proton density used to calculate the pressure.

Using a new a catalog of identified shock transitions, we updated three parametric bow shock models typically employed by the community. We list the best-fit parameters and model performance metrics in Table 1. Of the models we considered, we found that the Chao et al. (2002) model, when optimally parametrized, performs the best at describing MMS shock crossings. However, after refitting each model, the Chapman et al. (2004) model produced the highest performance. We improved the fit of the Chapman et al. (2004) by 17% in terms of $R^2$ score improvement whereas enhancement to the fits of the Jelínek et al. (2012) and Chao et al. (2002) models were more modest (7% for both). The largest difference in the fits was obtained for the standoff distance, which resulted in the value being more inward than that in the Chapman et al. (2004) model.

After updating the fitting parameters of each model, the predicted locations of all three models were much improved, but still struggled during rare or extreme solar wind conditions. Examining a select sample of bow shocks that were observed during extreme solar wind conditions, we found that MMS was observing real bow shock crossings where the Earth's nominal bow shock was warped by an extremely high or low density solar wind. Though not studied in our analysis, the dipole tilt has been shown to significantly affect the shape and location of the bow shock (e.g., Merka & Szabo, 2004) and may be especially important since MMS observations were limited close to the dayside equatorial plane. Investigating how the observed and modeled bow shock changes as a function of dipole tilt or at the flanks versus the subsolar point would make for interesting avenues of future work.

We also identified subsets of bow shocks categorized by their IMF clock angle (IMF North and South) and by the shock geometry (quasi-parallel and quasi-perpendicular) to individually fit the three studied parametric models. For IMF North versus IMF South bow shocks, we did not find any major differences in the model shapes. However, for quasi-perpendicular versus quasi-parallel bow shocks, we discovered that the models were better at predicting locations of quasi-parallel bow shocks than they are quasi-perpendicular bow shocks. Future work includes a more detailed analysis of the upstream and downstream parameters defining the IMF clock angle and shock geometry and how it fits in with the understanding of the configuration of the Parker Spiral.

With MMS observations, we were limited to bow shocks close to the equatorial plane. Future work can expand upon this analysis with higher latitude and nightside shock crossings. Subsequent investigations may benefit from

including shock crossings from various missions (e.g., THEMIS, Cluster, and Geotail) to cover a wider range of parameter space and to minimize the orbital effects and sampling of the solar cycle that each mission may introduce. Our work ultimately highlights the necessity of re-evaluating empirical modeling efforts with new observations as optimal parametrization appears to deviate up to 17% compared to the original model fit.

Furthermore, by inspecting the cases in which observed bow shocks had the strongest deviation from the model, we showed modeling efforts struggle to capture the shock location and shape during very weak or very intense drivers. This result suggests that future investigations could benefit from formulating models that are fitted exclusively to such conditions. Such models may be particularly useful in space weather since these rare drivers can be associated with solar transient phenomena such as coronal mass ejections or magnetic clouds.

## Conflict of Interest

The authors declare no conflicts of interest relevant to this study.

## Data Availability Statement

The Toy-Edens et al. (2024) catalog of plasma region labels in MMS can be downloaded from Zenodo (https://zenodo.org/records/11032322). MMS data is publicly available from the Science Data Center (https://lasp.colorado.edu/mms/sdc/public/). OMNI data (King & Papitashvili, 2020) and the IMP 8 bow shock catalog (Merka et al., 2022) can be accessed from NASA's Coordinated Data Analysis Web (CDAWeb, https://cdaweb.gsfc.nasa.gov). The list of bow shocks and associated OMNI solar wind parameters produced in this work are included as Supporting Information S1.

**Acknowledgments**
This work was funded by the NSF Geospace Environment Modeling (GEM) Grant 2225463 and NASA award 80NSSC24K0173. S.R. acknowledges support from Johns Hopkins University Applied Physics Laboratory independent R&D fund and the MMS Early Career Award 80NSSC25K7353. K.Y. is currently a MIT Lincoln Laboratory employee; no MIT Lincoln Laboratory funding or resources were used to produce the results/findings reported in this publication.

## References

An, X., Liu, T. Z., Bortnik, J., Osmane, A., & Angelopoulos, V. (2020). Formation of foreshock transients and associated secondary shocks. *The Astrophysical Journal*, *901*(1), 73. https://doi.org/10.3847/1538-4357/abaf03

Balogh, A., & Treumann, R. A. (2013). *Physics of collisionless shocks: Space plasma shock waves*. Springer Science & Business Media.

Battarbee, M., Ganse, U., Pfau-Kempf, Y., Turc, L., Brito, T., Grandin, M., et al. (2020). Non-locality of earth's quasi-parallel bow shock: Injection of thermal protons in a hybrid-vlasov simulation. *Annales Geophysicae*, *38*(3), 625–643. https://doi.org/10.5194/angeo-38-625-2020

Baumjohann, W., & Treumann, R. A. (1996). Basic space plasma physics. https://doi.org/10.1142/p015

Burch, J. L., Moore, T. E., Torbert, R. B., & Giles, B. L. (2015). Magnetospheric multiscale overview and science objectives. *Space Science Reviews*, *199*(1–4), 5–21. https://doi.org/10.1007/s11214-015-0164-9

Cairns, I. H., & Lyon, J. G. (1995). MHD simulations of Earth's bow shock at low Mach numbers: Standoff distances. *Journal of Geophysical Research*, *100*(A9), 17173–17180. https://doi.org/10.1029/95JA00993

Case, N. A., & Wild, J. A. (2012). A statistical comparison of solar wind propagation delays derived from multispacecraft techniques. *Journal of Geophysical Research: Space Physics*, *117*(A2). https://doi.org/10.1029/2011JA016946

Cash, M. D., Witters Hicks, S., Biesecker, D. A., Reinard, A. A., de Koning, C. A., & Weimer, D. R. (2016). Validation of an operational product to determine l1 to Earth propagation time delays. *Space Weather*, *14*(2), 93–112. https://doi.org/10.1002/2015SW001321

Chao, J. K., Wu, D. J., Lin, C. H., Yang, Y. H., Wang, X. Y., Kessel, M., et al. (2002). Models for the size and shape of the Earth's magnetopause and bow shock. In L.-H. Lyu (Ed.), *Space weather study using multipoint techniques*. (p. 127).

Chapman, J. F., & Cairns, I. H. (2003). Three-dimensional modeling of Earth's bow shock: Shock shape as a function of Alfvén Mach number. *Journal of Geophysical Research (Space Physics)*, *108*(A5), 1174. https://doi.org/10.1029/2002JA009569

Chapman, J. F., Cairns, I. H., Lyon, J. G., & Boshuizen, C. R. (2004). MHD simulations of Earth's bow shock: Interplanetary magnetic field orientation effects on shape and position. *Journal of Geophysical Research (Space Physics)*, *109*(A4), A04215. https://doi.org/10.1029/2003JA010235

Dungey, J. W. (1961). Interplanetary magnetic field and the auroral zones. *Physical Review Letters*, *6*(2), 47–48. https://doi.org/10.1103/PhysRevLett.6.47

Henderson, M. G., Morley, S. K., & Burch, J. L. (2022). Mms 4 Magnetic Ephemeris and Coordinates (MEC) and support (Tsyganenko 1989 model, dynamic conditions), level 2 (l2), survey mode, 30 s data. *NASA Space Physics Data Facility*. https://doi.org/10.48322/552N-ER81

Holzer, R. E., & Slavin, J. A. (1978). Magnetic flux transfer associated with expansions and contractions of the dayside magnetosphere. *Journal of Geophysical Research*, *83*(A8), 3831–3839. https://doi.org/10.1029/JA083iA08p03831

Jelínek, K., Němeček, Z., & Šafránková, J. (2012). A new approach to magnetopause and bow shock modeling based on automated region identification. *Journal of Geophysical Research (Space Physics)*, *117*(A5), A05208. https://doi.org/10.1029/2011JA017252

Jeřáb, M., Němeček, Z., Šafránková, J., Jelínek, K., & Měrka, J. (2005). Improved bow shock model with dependence on the IMF strength. *Planetary and Space Science*, *53*(1–3), 85–93. https://doi.org/10.1016/j.pss.2004.09.032

Johlander, A., Battarbee, M., Turc, L., Ganse, U., Pfau-Kempf, Y., Grandin, M., et al. (2022). Quasi-parallel shock reformation seen by magnetospheric multiscale and ion-kinetic simulations. *Geophysical Research Letters*, *49*(2), e2021GL096335. https://doi.org/10.1029/2021gl096335

Kajdič, P., Blanco-Cano, X., Omidi, N., Rojas-Castillo, D., Sibeck, D. G., & Billingham, L. (2017). Traveling foreshocks and transient foreshock phenomena. *Journal of Geophysical Research: Space Physics*, *122*(9), 9148–9168. https://doi.org/10.1002/2017ja023901

Karlsson, T., Raptis, S., Trollvik, H., & Nilsson, H. (2021). Classifying the magnetosheath behind the quasi-parallel and quasi-perpendicular bow shock by local measurements. *Journal of Geophysical Research: Space Physics*, *126*(9), e2021JA029269. https://doi.org/10.1029/2021JA029269

King, J. H., & Papitashvili, N. E. (2005). Solar wind spatial scales in and comparisons of hourly wind and ACE plasma and magnetic field data. *Journal of Geophysical Research (Space Physics)*, *110*(A2), A02104. https://doi.org/10.1029/2004JA010649

King, J. H., & Papitashvili, N. E. (2020). OMNI 1-min data set [Dataset]. *NASA Space Physics Data Facility*. https://doi.org/10.48322/45BB-8792

Lalti, A., Khotyaintsev, Y. V., Dimmock, A. P., Johlander, A., Graham, D. B., & Olshevsky, V. (2022). A database of MMS bow shock crossings compiled using machine learning. *Journal of Geophysical Research: Space Physics*, *127*(8), e2022JA030454. https://doi.org/10.1029/2022JA030454

LaMoury, A. T., Hietala, H., Plaschke, F., Vuorinen, L., & Eastwood, J. P. (2021). Solar wind control of magnetosheath jet formation and propagation to the magnetopause. *Journal of Geophysical Research: Space Physics*, *126*(9), e2021JA029592. https://doi.org/10.1029/2021JA029592

Merka, J., & Szabo, A. (2004). Bow shock's geometry at the magnetospheric flanks. *Journal of Geophysical Research: Space Physics*, *109*(A12). https://doi.org/10.1029/2004JA010567

Merka, J., Szabo, A., Narock, T. W., King, J. H., Paularena, K. I., & Richardson, J. D. (2003). A comparison of IMP 8 observed bow shock positions with model predictions. *Journal of Geophysical Research: Space Physics*, *108*(A2). https://doi.org/10.1029/2002JA009384

Merka, J., Szabo, A., Paularena, K., Richardson, J., & Narock, T. (2022). Imp 8 bow shock crossings [Dataset]. *NASA/WIND/IMP 8 mission*. https://doi.org/10.48322/753J-G416

Newville, M., Stensitzki, T., Allen, D. B., & Ingargiola, A. (2015). LMFIT: Non-linear least-square minimization and curve-fitting for python. *Zenodo*. https://doi.org/10.5281/zenodo.11813

Nguyen, G., Aunai, N., Michotte de Welle, B., Jeandet, A., Lavraud, B., & Fontaine, D. (2022). Massive multi-mission statistical study and analytical modeling of the earth's magnetopause: 1. A gradient boosting based automatic detection of near-earth regions. *Journal of Geophysical Research: Space Physics*, *127*(1), e2021JA029773. https://doi.org/10.1029/2021JA029773

Olshevsky, V., Khotyaintsev, Y. V., Lalti, A., Divin, A., Delzanno, G. L., Anderzén, S., et al. (2021). Automated classification of plasma regions using 3d particle energy distributions. *Journal of Geophysical Research: Space Physics*, *126*(10), e2021JA029620. https://doi.org/10.1029/2021ja029620

Perri, S., Bykov, A., Fahr, H., Fichtner, H., & Giacalone, J. (2022). Recent developments in particle acceleration at shocks: Theory and observations. *Space Science Reviews*, *218*(4), 26. https://doi.org/10.1007/s11214-022-00892-5

Pollock, C., Moore, T., Jacques, A., Burch, J., Gliese, U., Saito, Y., et al. (2016). Fast plasma investigation for magnetospheric multiscale. *Space Science Reviews*, *199*(1), 331–406. https://doi.org/10.1007/s11214-016-0245-4

Raptis, S., Karlsson, T., Plaschke, F., Kullen, A., & Lindqvist, P.-A. (2020). Classifying magnetosheath jets using MMS: Statistical properties. *Journal of Geophysical Research: Space Physics*, *125*(11), e2019JA027754. https://doi.org/10.1029/2019JA027754

Raptis, S., Karlsson, T., Vaivads, A., Pollock, C., Plaschke, F., Johlander, A., et al. (2022). Downstream high-speed plasma jet generation as a direct consequence of shock reformation. *Nature communications*, *13*(1), 598. https://doi.org/10.1038/s41467-022-28110-4

Shue, J. H., Chao, J. K., Fu, H. C., Russell, C. T., Song, P., Khurana, K. K., & Singer, H. J. (1997). A new functional form to study the solar wind control of the magnetopause size and shape. *Journal of Geophysical Research*, *102*(A5), 9497–9512. https://doi.org/10.1029/97JA00196

Shue, J.-H., Chen, Y.-S., Hsieh, W.-C., Nowada, M., Lee, B. S., Song, P., et al. (2011). Uneven compression levels of Earth's magnetic fields by shocked solar wind. *Journal of Geophysical Research: Space Physics*, *116*(A2). https://doi.org/10.1029/2010JA016149

Torbert, R. B., Russell, C. T., Magnes, W., Ergun, R. E., Lindqvist, P.-A., LeContel, O., et al. (2014). The FIELDS instrument suite on MMS: Scientific objectives, measurements, and data products. *Space Science Reviews*, *199*(1–4), 105–135. https://doi.org/10.1007/s11214-014-0109-8

Toy-Edens, V., Mo, W., Raptis, S., & Turner, D. L. (2024). Classifying 8 years of MMS dayside plasma regions via unsupervised machine learning. *Journal of Geophysical Research: Space Physics*, *129*(6), e2024JA032431. https://doi.org/10.1029/2024JA032431

Treumann, R. (2009). Fundamentals of collisionless shocks for astrophysical application, 1. Non-relativistic shocks. *Astronomy and Astrophysics Review*, *17*(4), 409–535. https://doi.org/10.1007/s00159-009-0024-2

Turner, D. L., Wilson, L. B., III., Goodrich, K. A., Madanian, H., Schwartz, S. J., Liu, T. Z., et al. (2021). Direct multipoint observations capturing the reformation of a supercritical fast magnetosonic shock. *The Astrophysical Journal Letters*, *911*(2), L31. https://doi.org/10.3847/2041-8213/abec78

Wilson, L. B., III., Brosius, A. L., Gopalswamy, N., Nieves-Chinchilla, T., Szabo, A., Hurley, K., et al. (2021). A quarter century of wind spacecraft discoveries. *Reviews of Geophysics*, *59*(2), e2020RG000714. https://doi.org/10.1029/2020RG000714

Yeakel, K. L., Cohen, I., & Turner, D. L. (2025). Variability of earth's magnetopause and bow shock locations modeled via multi-decade solar. *Wind Observations*, *52*(10), e2025GL115462. https://doi.org/10.1029/2025GL115462